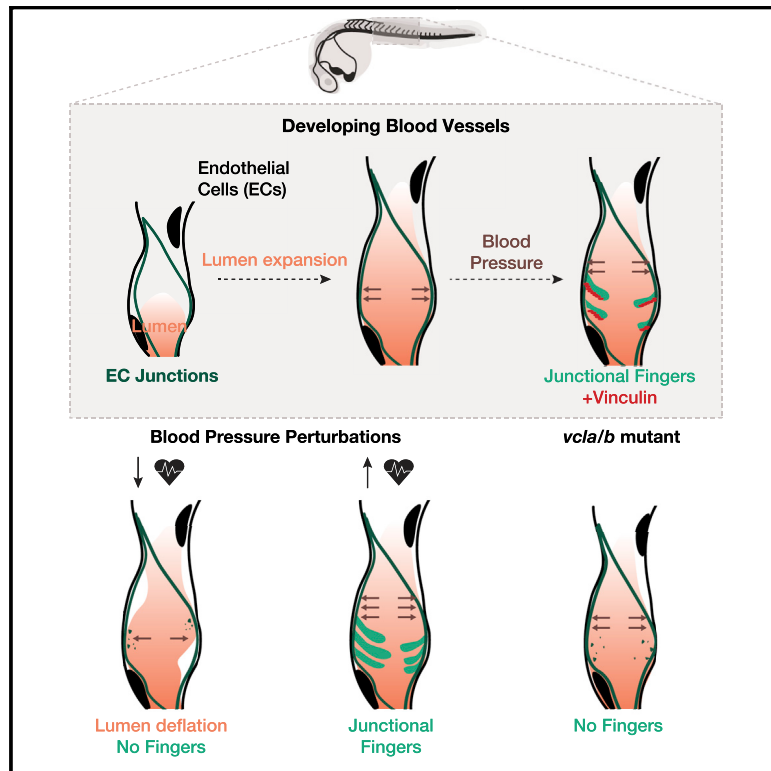# Cell Reports

Vinculin controls endothelial cell junction dynamics during vascular lumen formation

Graphical abstract

Authors

Maria P. Kotini, Miesje M. van der Stoel, Jianmin Yin, ..., Markus Affolter, Stephan Huveneers, Heinz-Georg Belting

Correspondence

s.huveneers@amsterdamumc.nl (S.H.), heinz-georg.belting@unibas.ch (H.-G.B.)

In brief

Kotini et al. investigate junctional dynamics during angiogenic lumen formation. Finger-shaped junctions containing the mechanotransduction protein vinculin are formed in response to blood pressure. Vinculin is required for finger formation and maintenance. Junctional fingers present an *in vivo* paradigm to study junctional dynamics in relation to extrinsic forces.

Highlights

- Endothelial cells form finger-shaped junctions during angiogenic sprouting

- Junctional fingers appear in response to incoming blood pressure

- Vinculin is localized at junctional fingers during lumen inflation

- Finger formation and maintenance require vinculin

Cell Reports

Article

Vinculin controls endothelial cell junction dynamics during vascular lumen formation

Maria P. Kotini,[1,5] Miesje M. van der Stoel,[2,5] Jianmin Yin,[1] Mitchell K. Han,[3] Bettina Kirchmaier,[4] Johan de Rooij,[3] Markus Affolter,[1,6] Stephan Huveneers,[2,6,*] and Heinz-Georg Belting[1,6,7,*]

[1]Biozentrum der Universität Basel, Spitalstrasse 41, 4056 Basel, Switzerland
[2]Amsterdam UMC, Department of Medical Biochemistry, Amsterdam Cardiovascular Sciences, University of Amsterdam, Meibergdreef 9, 1105 AZ Amsterdam, the Netherlands
[3]Department of Molecular Cancer Research, Center for Molecular Medicine, University Medical Center Utrecht, Stratenum 3.231, Universiteitsweg 100, 3584 CG Utrecht, the Netherlands
[4]Institute for Cell Biology and Neuroscience, Biologicum/Campus Riedberg, Goethe-Universität Frankfurt Am Main, 60438 Frankfurt Am Main, Germany
[5]These authors contributed equally
[6]Senior author
[7]Lead contact
*Correspondence: s.huveneers@amsterdamumc.nl (S.H.), heinz-georg.belting@unibas.ch (H.-G.B.)
https://doi.org/10.1016/j.celrep.2022.110658

SUMMARY

Blood vessel morphogenesis is driven by coordinated endothelial cell behaviors. Active remodeling of cell-cell junctions promotes cellular plasticity while preserving vascular integrity. Here, we analyze the dynamics of endothelial adherens junctions during lumen formation in angiogenic sprouts *in vivo*. Live imaging in zebrafish reveals that lumen expansion is accompanied by the formation of transient finger-shaped junctions. Junctional fingers are positively regulated by blood pressure, whereas flow inhibition prevents their formation. Using fluorescent reporters, we show that junctional fingers contain the mechanotransduction protein vinculin. Furthermore, genetic deletion of vinculin prevents finger formation, a junctional defect that could be rescued by transient endothelial expression of vinculin. Our findings suggest a mechanism whereby lumen expansion leads to an increase in junctional tension, triggering recruitment of vinculin and formation of junctional fingers. We propose that endothelial cells employ force-dependent junctional remodeling to counteract external forces in order to maintain vascular integrity during sprouting angiogenesis.

INTRODUCTION

The cardiovascular system is essential for vertebrate development and homeostasis as it serves as a transport system to deliver and exchange gas and solutes in all parts of the body. The cardiovascular system is the first organ to form during embryonic development, and it adapts to the needs of the growing embryo by expansion of the vascular network (Hogan and Schulte-Merker, 2017; Potente et al., 2011). To a large extent, this is achieved by the formation of new vessels in a process called sprouting angiogenesis.

Blood vessel formation by angiogenesis occurs in discrete steps of sprout outgrowth, lumen formation, and sprout fusion. At the cellular level, these morphogenetic processes are achieved by numerous cell activities, such as endothelial cell migration, cell rearrangements, and cell shape changes, which in turn are driven by a complex array of intracellular activities as well as dynamic cell-cell and cell-extracellular matrix (ECM) interactions (reviewed by Betz et al., 2016; Szymborska and Gerhardt, 2018). During angiogenesis, multiple morphogenetic processes occur simultaneously, posing a particular challenge to

endothelial cell-cell junctions. Fine-tuned regulation of cell-cell adhesion is required to permit endothelial cell migration and rearrangements while maintaining the vascular seal to prevent leakage or hemorrhage.

Endothelial cell-cell junctions play a central role in many aspects of endothelial cell biology. They regulate not only cell-cell adhesion and vascular permeability but also proliferation, survival, shape, and motility, and they are involved in the modulation of signaling pathways and transcriptional regulation (reviewed by Komarova et al., 2017; Lampugnani et al., 2017; Wallez and Huber, 2008). In addition to forming a structural link between neighboring endothelial cells, the junctions can act as sensors to adapt to forces that are derived from the actomyosin cytoskeleton or the vascular hemodynamic microenvironment (Huveneers et al., 2012; Lagendijk et al., 2017; Tzima et al., 2005; Liu et al., 2010). During vascular morphogenesis, endothelial cells are exposed to mechanical forces generated by matrix stiffness, fluid shear stress, blood pressure, actomyosin contractility, and junctional tension (Duchemin et al., 2019; Hoefer et al., 2013; Roman and Pekkan, 2012). Recent work has shown that endothelial cell-cell junctions play an important role
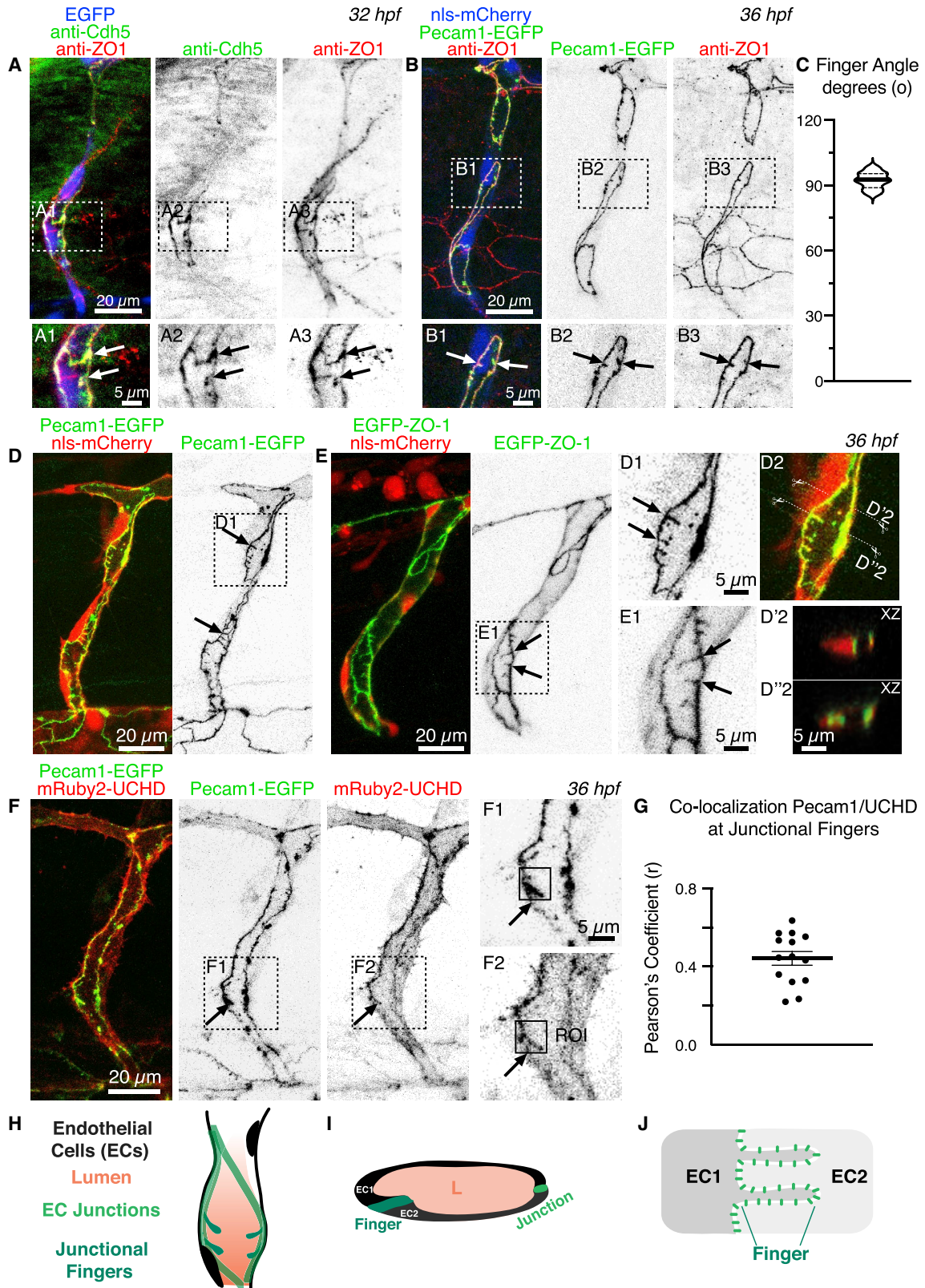
(legend on next page)

in mechanical force sensing and force transmission, specifically by changing the organization of vascular endothelial (VE)-cadherin-based junctions (Angulo-Urarte et al., 2020; Baeyens and Schwartz, 2016; Conway et al., 2013). Tension on the VE-cadherin/β-catenin/α-catenin complex recruits the mechanotransduction protein vinculin, which in turn protects the endothelial junctions during their remodeling (Huveneers et al., 2012). Force-dependent signals are transmitted through the VE-cadherin complex and via junctional vinculin recruitment enable collective endothelial responses *in vitro* (Barry et al., 2015).

Recent work in zebrafish embryos showed that the adhesion molecule VE-cadherin transduces intracellular actomyosin contractility to endothelial cell-cell junctions *in vivo* (Lagendijk et al., 2017) and also participates in force-generating processes during endothelial cell rearrangements (Paatero et al., 2018). Here, we have studied how endothelial cells respond to mechanical stress imposed in a changing environment. To this end, we examine endothelial cell-cell junctions during angiogenic lumen expansion, which is accompanied with an acute increase in blood pressure within the sprouting intersegmental vessels (ISVs). Our studies reveal junctional structures within angiogenic sprouts, which we call junctional fingers. These junctional fingers form transiently in response to increased pressure and recruit vinculin. Genetic analyses reveal that vinculin is required for junctional finger formation. Taken together, our studies indicate that endothelial cells protect their cell-cell contact against mechanical stress by forming junctional fingers, thereby maintaining sprout integrity during lumen expansion.

RESULTS

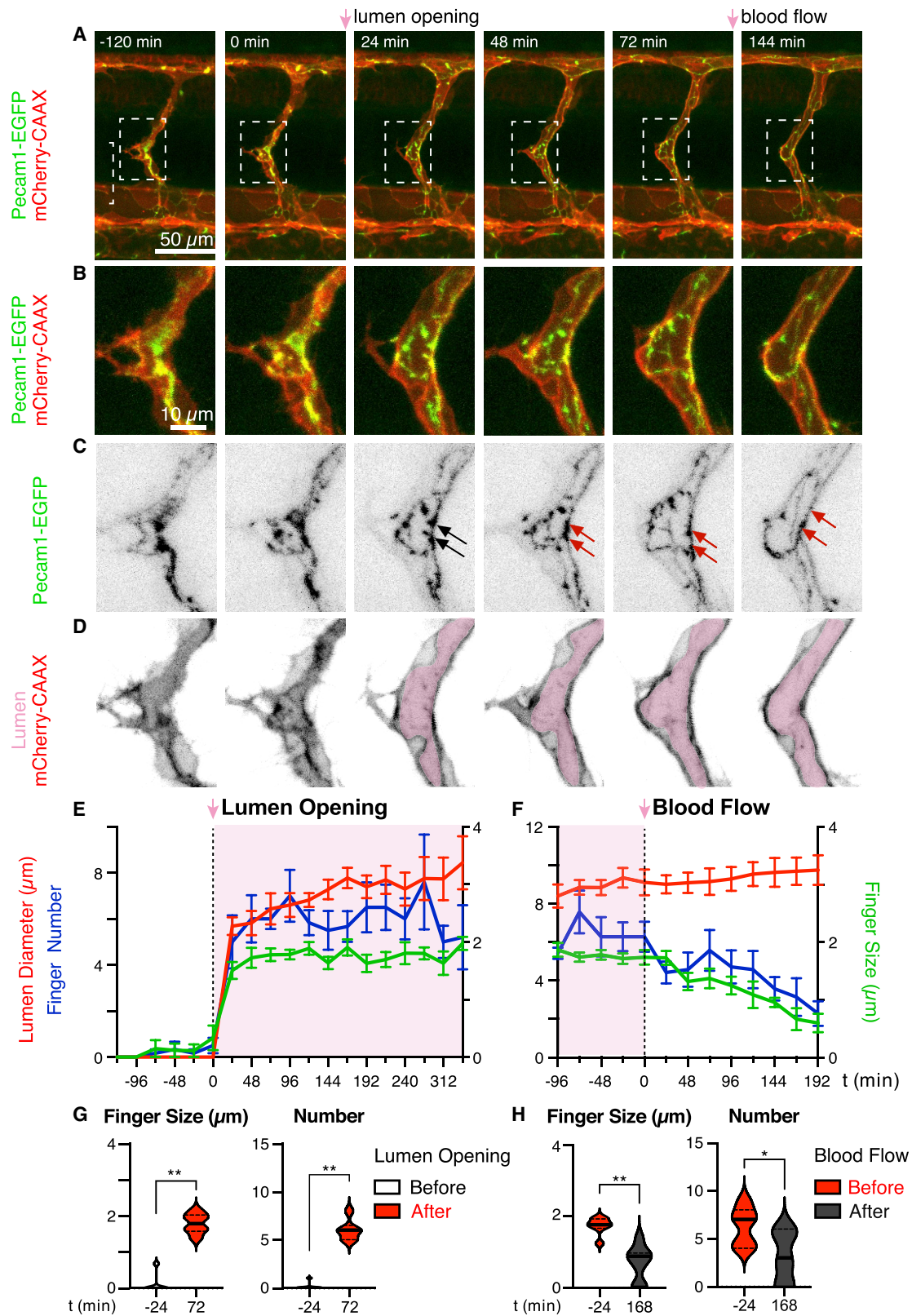### Endothelial junctional fingers appear during vascular lumen formation *in vivo*

During blood vessel formation, endothelial junctions play permissive as well as active roles, driving cell rearrangements and cell elongation while maintaining vascular integrity at the same time (reviewed by Fonseca et al., 2020; Okuda and Hogan, 2020). Furthermore, endothelial junctions are thought to sense and transmit mechanical forces and thus regulate the collective endothelial response to changes in blood flow or pressure, which

occur at the onset of blood flow in a newly formed vessel. To investigate the response of endothelial cell-cell junctions to changes in blood pressure, we followed junctional dynamics in zebrafish ISVs during the onset of lumen formation around 28–36 h postfertilization (hpf). Immunofluorescent analyses of the adherens junction protein VE-cadherin (Cdh5) and tight junction protein zonula occludens-1 (ZO-1/TJP1) revealed finger-shaped structures (Figure 1A), which emanated from the cell-cell contact interface, confirming our previous observations (Sauteur et al., 2014). These junctional fingers appeared perpendicular to the originating junction with an angle of around 90° (Figure 1C). To check whether these junctional fingers are specifically formed by VE-cadherin-based adhesions or represented more general junctional structures, we analyzed the localization of platelet endothelial cell adhesion molecule-1 (Pecam1) using a transgenic reporter (*Tg(fli1a:pecam1a-EGFP)^ncv27*), followed by immunofluorescent analysis of ZO-1 (Figure 1B). We found that junctional fingers also contained Pecam1 and colocalized with ZO-1, indicating that several types of cell-cell adhesion complexes localize at sites of junctional fingers.

Because fixation of zebrafish embryos for immunofluorescence disrupts blood flow and can affect blood vessel morphology, we wanted to verify the existence of junctional fingers by live imaging using the above-mentioned Pecam1 reporter (Figures 1D, 1D1, and 1D2) as well as the ZO-1 reporter *Tg(UAS:EGFP-hZO1)^ubs5* (Figures 1E and 1E1) and the VE-cadherin reporter *TgBAC(ve-cad:ve-cadTS)^uq11bh* (Figures 1A and 1A1). These live-imaging experiments confirmed the presence of ZO-1, Pecam1, and VE-cadherin-positive fingers in the lumenized ISVs (Figures 1A, 1B, 1D, 1E, and S1A) and that junctional fingers appear perpendicular to the blood vessel long axis (Figures 1D2, 1D'2, and 1D''2). Features of junctional fingers, such as their size and number in the ISVs, were comparable for the various endogenous junctional molecules and the different junctional marker lines (Figures S1B–S1E). Furthermore, junctional fingers in live embryos appeared more prominent and larger compared with those observed in fixed embryos, suggesting that they are sensitive to the loss of blood pressure or fixation. Because cell-cell junctions are physically connected to the actin cytoskeleton, we next tested whether junctional fingers colocalize with mRuby2-UCHD, which labels stabilized

Figure 1. Endothelial junction fingers are formed by distinct junctional proteins

(A and B) Confocal images of intersegmental blood vessels (ISVs) in the trunk of fixed zebrafish embryos at 32 hpf (A) and 36 hpf (B). (A) Whole-mount immunofluorescence staining using anti-Cdh5 (VE-cadherin) and anti-ZO-1 in Tg(*fli1a:EGFP*) embryos is shown. Scale bar, 20 μm. (A1–A3) Zoom-in images of the outlined boxes show junctional fingers containing VE-cadherin and ZO-1 (black arrows). Scale bar, 5 μm. (B) Whole-mount immunofluorescence staining using anti-ZO-1 in Tg(*fli1a:nls-mCherry;fli1a:pecam1a-EGFP*) embryos is shown. Scale bar, 20 μm. (B1–B3) Zoom-in images of the outlined boxes in (B) show the presence of Pecam1 and ZO-1 at junctional fingers between endothelial cells. Scale bar, 5 μm.

(C) Distribution of the mean angle of junctional fingers (n = 17 embryos).

(D and E) Confocal images of ISVs in the trunk of zebrafish embryos at 36 hpf. (D) GFP[+] signal shows the junctional molecule Pecam1 and RFP[+] signal marks endothelial cell nuclei in *Tg(fli1a:nls-mCherry;fli1a:pecam1a-EGFP)* embryos. Scale bar, 20 μm. (E) GFP[+] signal marks the junctional molecule ZO-1, and RFP[+] signal indicates endothelial cell nuclei in *Tg(fli1a:nls-mCherry;fli1a:gal4ff;UAS:EGFP-ZO-1)* embryos. Scale bar, 20 μm. (D1 and E1) Zoom-in images of the outlined boxes in (D) and (E) are shown; black arrows indicate the presence of Pecam1, ZO-1, and Cdh5 at junctional fingers. Scale bars, 5 μm. (D2–D''2) XZ representation of EC junctions in (D'2) or junctional finger in (D''2) is shown.

(F) GFP[+] signal shows the junctional molecule Pecam1 and RFP[+] signal marks the F-actin cytoskeleton in *Tg(fli1a:gal4ff;UAS:mRuby2-UCHD;fli1a:pecam1a-EGFP)* embryos. Scale bar, 20 μm. (F1 and F2) Zoom-in images of the outlined boxes in (F) are shown. Black arrow indicates the presence of F-actin at a junctional finger. Scale bar, 5 μm.

(G) Co-localization analysis (Pearson's coefficient, r) of Pecam-1 signal and UCHD at fingers (n = 14 embryos).

(H and I) Schematic representation of junctional fingers appearing in an ISV during lumen formation (H, lateral view; I, transverse view).

(J) Schematic representation of junctional fingers at the interface of two endothelial cells.

See also Figure S1.

A
Pecam1-EGFP
mCherry-CAAX

↓ lumen opening   ↓ blood flow

-120 min   0 min   24 min   48 min   72 min   144 min

50 μm

B
Pecam1-EGFP
mCherry-CAAX

10 μm

C
Pecam1-EGFP

D
Lumen
mCherry-CAAX

E   ↓ Lumen Opening

F   ↓ Blood Flow

G   Finger Size (μm)   Number

Lumen Opening
☐ Before
■ After

H   Finger Size (μm)   Number

Blood Flow
■ Before
■ After

(legend on next page)

F-actin fibers (Burkel et al., 2007). Live imaging revealed that Pecam1-positive junctional fingers were also marked by mRuby2-UCHD and that Pecam1 and F-actin partially colocalized at junctional fingers (Figures 1F and 1G). Taken together, this set of experiments indicates that junctional fingers are formed during angiogenic sprouting in the developing ISVs (Figures 1H–1J) and contain multiple junctional proteins, including VE-cadherin, ZO-1, and Pecam1, which can interact with the endothelial F-actin cytoskeleton.

Since junctional fingers are particularly prevalent in newly lumenized blood vessels (30–36 hpf), we monitored the appearance of junctional fingers during this time window by *in vivo* time-lapse imaging using the Pecam1-EGFP reporter. Before ISV lumen opening, we observed the presence of dense junctional clusters but no junctional fingers (Figures 2A–2E, time points −120 and 0 min; Video S1). By contrast, the junctional fingers readily formed upon lumen opening (black arrows, Figures 2A–2E and 2G, from time point 24 min onwards; Figure S2; Video S2). Over time, the size of the fingers fluctuated, and they eventually regressed once the ISV lumens were connected upon anastomosis, and when mostly stable, linear-oriented junctions were established (red arrows, Figures 2A–2D, 2F, and 2H, time points 48, 72, and 144 min; Figure S2; Video S1). These findings show that junctional fingers are transient structures, which form during lumen formation prior to commencement of blood flow (Figures 2E and S2). When blood flow is established, the junctional fingers disappear (Figures 2F and S2). These correlations suggest a close relationship between hemodynamic forces and junctional finger formation.

Hemodynamic forces control junctional fingers

Previous studies have shown that ISVs can lumenize in different ways. Cell membrane invagination leads to the formation of a lumen within a cell (Herwig et al., 2011). This process, also called transcellular lumen formation, is driven by blood pressure and thus requires blood flow (Gebala et al., 2016; Herwig et al., 2011; Lenard et al., 2013). In the absence of blood flow, ISV lumens are formed by cord hollowing, which is driven by endothelial cell rearrangements and gives rise to multicellular tubes (Herwig et al., 2011). Because ISV sprouting is initiated just prior to the start of embryonic blood flow, both modes of lumen formation may occur in these vessels (Gebala et al., 2016; Herwig et al., 2011; reviewed by Phng and Belting, 2021).

Because of the correlation between the occurrence of junctional fingers and lumen formation on one hand and the relationship between blood flow and lumen inflation on the other, we wanted to address to what extent the formation of junctional fingers is dependent on hemodynamic forces. We applied different drug treatments to modulate blood flow in embryos expressing transgenic endothelial reporters for cell-cell junctions (*fli1a:pecam1a-EGFP*) and cell membranes (*fli1a:mCherry-CAAX*). Tricaine treatment, which reduces cardiac contraction and consequently inhibits blood flow and blood pressure (Lagendijk et al., 2017; Lenard et al., 2013), led to a decrease in size and number of fingers compared with controls (vehicle-treated embryos; Figures 3A, 3B, 3E, 3G, and 3H). By contrast, norepinephrine (NE) treatment, which raises the heart rate and increases the hemodynamic forces in zebrafish blood vessels (Chen et al., 2012; De Luca et al., 2014), increased the size and number of junctional fingers (Figures 3C, 3D, and 3F–3H).

To investigate whether changes in hemodynamic forces directly affect junctional finger dynamics, we next performed sequential treatments. Junctional clusters appeared before lumen opening of the ISV in zebrafish embryos (Figures 4A and 4A1–4A3, time point 0; Video S2), and junctional fingers were formed during ISV lumenization (Figure 4A, time points 20 and 40 min), confirming our earlier findings (Figure 2). Subsequent treatment of the same embryo with NE to promote blood flow induced junctional clustering and finger formation in the lumenized ISV (Figures 4B, 4B1–4B3, and 4D–4F, time points 120 and 160 min). Follow-up treatment with tricaine immediately caused lumen regression and destabilized junctional fingers (Figures 4C, 4C1–4C3, and 4D–4F, time points 240–280 min). Administration of the treatments in reverse order showed results consistent with the above observations (Figure 4) and, more specifically, first a regression of fingers in ISVs (upon tricaine addition) and subsequently a re-emergence of fingers (upon norepinephrine addition; Figures S3A–S3D; Video S3). Taken together, these experiments show that junctional fingers form in response to an increase in blood flow or blood pressure and that thus they represent dynamic structures that directly respond to changes in hemodynamic forces.

Junctional fingers represent regions of elevated junctional tension

The observation that junctional fingers form in response to increased blood pressure suggests that their formation may be

---

Figure 2. Junctional fingers assemble upon lumen opening

(A–D) Still images from a time-lapse movie of a Tg(*kdrl:mCherry-CAAX;fli1a:pecam1a-EGFP*) embryo starting at 32 hpf. GFP$^+$ signal marks the endothelial cell-cell junctions, and mCherry$^+$ signal demarcates endothelial cell plasma membranes. First two time points (−120 and 0 min) display a representative ISV before lumen opening. The following time points (24–72 min) visualize the ISV after lumen opening, and the last time point (144 min) shows the ISV after anastomosis and establishment of blood flow (see also example 3, Figure S2C). (A) Overview images are shown. Scale bar, 50 μm. (B) Zoom-in images of the outlined boxes in (A) are shown. Scale bar, 10 μm. (C) Inverted contrast of the Pecam1-EGFP channel from (B) is shown. Right before lumen opening, junctional accumulation is evident at future sites of junctional fingers. After lumen opening, junctional fingers assemble (black arrows) and regress (red arrows) over time. (D) Inverted contrast of mCherry-CAAX from (B) shows lumen opening. Pink pseudo-color indicates the vascular lumen.

(E and F) Junctional finger dynamics during lumen opening (E) and upon establishment of blood flow (F). Analyses show the finger size ± SE, finger number ± SE, and lumen diameter ± SE from Tg(*kdrl:mCherry-CAAX;fli1a:pecam1a-EGFP*) embryos (n = 7); pink boxes indicate the time period when lumen opens but without blood flow, during which junctional fingers appear.

(G) Junctional finger analysis at distinct time points before and after lumen opening (−24 and 72 min).

(H) Junctional finger analysis at distinct time points before and after establishment of blood flow (−24 and 168 min).

(G and H) n = 7 embryos; *p < 0.05; **p < 0.01 (one-way ANOVA).

See also Figure S2 and Video S1.
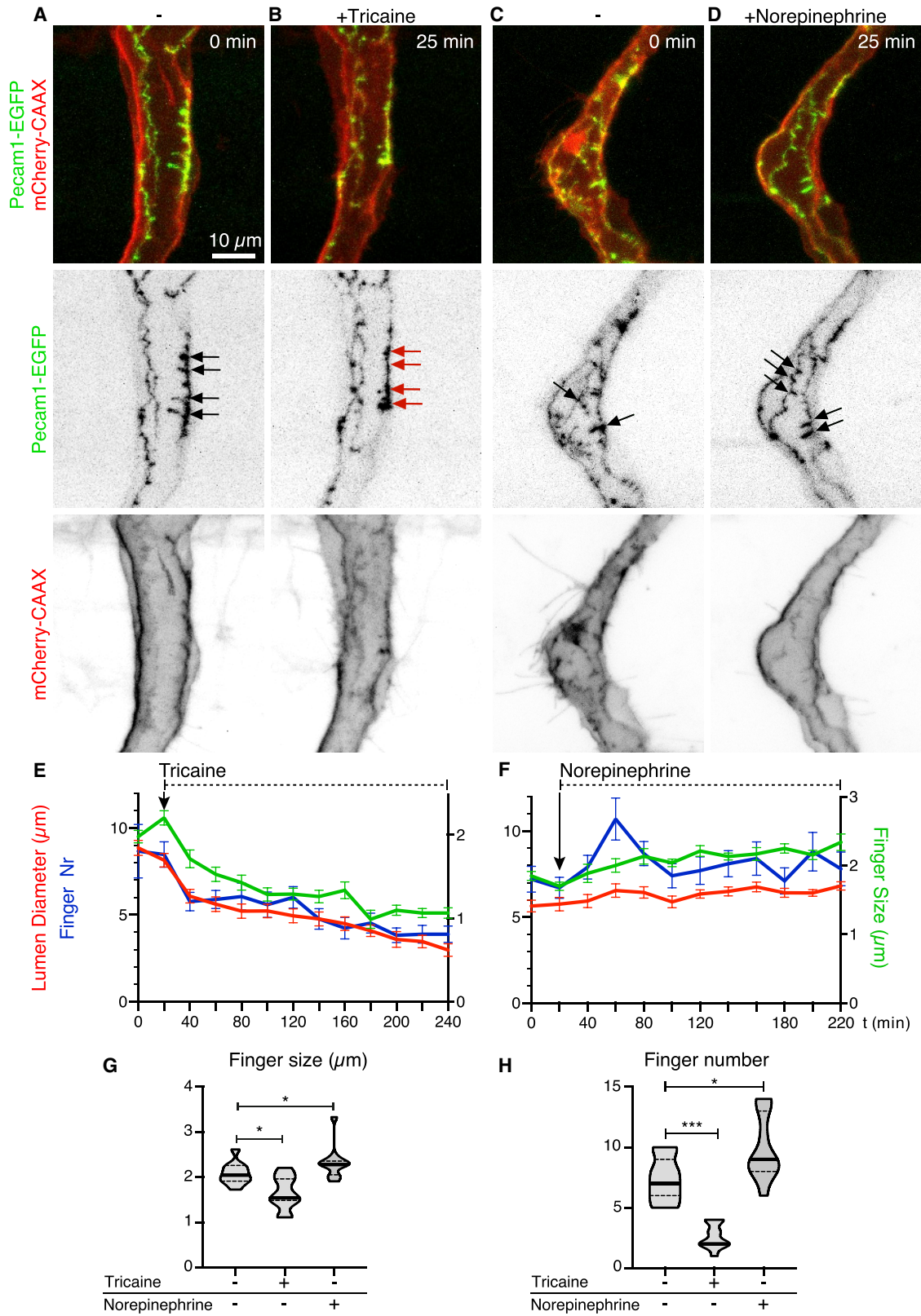
(legend on next page)

triggered by mechanical forces. We therefore reasoned that an acute increase in blood pressure might increase tensile forces exerted on endothelial cell-cell junctions. Previous work in human umbilical vein endothelial cells (HUVECs) has shown that increased tension on the VE-cadherin complex induces unfolding of α-catenin, exposing its cryptic vinculin binding site (Huveneers et al., 2012; Yao et al., 2014). The subsequent junctional recruitment of vinculin reinforces the connection of VE-cadherin with the actin cytoskeleton and protects junctions during their force-dependent remodeling (Huveneers et al., 2012). Since junctional localization of vinculin corresponds to sites of increased tension, we wanted to test whether vinculin is localized at junctional fingers in ISVs. To achieve this, we transiently expressed an mCherry-vinculin fusion protein (*kdrl:mCherry-vinculin*) in the endothelium of transgenic *fli1a:pecam1a-EGFP* embryos. Using live imaging, we observed that vinculin localizes at the junctional fingers (black arrows, Figures 5A and 5B). Moreover, time-lapse imaging showed that vinculin localization is dynamic and follows the turnover of the Pecam1-positive junctional fingers. Although the majority of vinculin was distributed in the cytoplasm, upon formation of junctional fingers, vinculin became enriched at these structures and was most prominent once junctional fingers had reached their maximum size (Figures 5B and 5C; Video S4). This close correlation between junctional finger formation and vinculin accumulation indicates that junctional fingers represent regions of elevated tension at the junctional interface. Furthermore, these observations suggest that vinculin may play a role in the formation and/or function of junctional fingers.

Vinculin is required for ISV morphogenesis

To investigate whether vinculin plays a role in endothelial junctional finger formation, we took a genetic loss-of-function approach. The zebrafish genome contains two *vinculin* paralogs, *vinculin a* (*vcla*) and *vinculin b* (*vclb*), which share high-sequence homology with their mammalian orthologs, including human *VCL* (87% and 86% identical amino acids, respectively; Han et al., 2017). In addition, both *vcla* and *vclb* paralogs are expressed in endothelial cells in zebrafish (Figure S4A; Lawson et al., 2020). Zebrafish loss-of-function mutants for *vcla* and *vclb* have previously been published (Fukuda et al., 2019; Cheng et al., 2016; El-Brolosy et al., 2019; Han et al., 2017).

To investigate the consequence of vinculin depletion for sprouting angiogenesis, we employed the *vcl* knockout models generated by Han et al. (2017; Figures S4B–S4D) and crossed the *vcla*[hu10818] homozygous; *vclb*[hu11202] heterozygous (*vcla*^{−/−}; *vclb*^{+/−}) fish into the *Tg(fli1a:EGFP*[y1]*)* vascular reporter line. Live imaging of the offspring revealed vascular defects in angio-

genic ISV sprouts of *vcl* double-knockout (*vcla*^{−/−}; *vclb*^{−/−}) and *vcl* heterozygous (*vcla*^{−/−}; *vclb*^{+/−}) embryos from 28 hpf onwards (Figures S5 and S6; Videos S5 and S6). In wild-type (*vcla*^{+/+}; *vclb*^{+/+}) embryos, ISVs sprouted out of the dorsal aorta (DA) from and anastomosed once tip cells reached the dorsolateral roof of the neural tube (Figures S5A and S5A1). In contrast, *vclb* heterozygous (*vcla*^{−/−};*vclb*^{+/−}; Figures S5B and S5B1) and *vcl* double-knockout (*vcla*^{−/−};*vclb*^{−/−}) embryos (Figures S5C and S5C1) showed a retardation in ISV sprouting evidenced by a decreased ISV length and an increased ISV diameter at 28 hpf (Figures S5D–S5F, S6F, and S6G; Videos S5 and S6). Furthermore, we observed that increasing loss of *vcla/b* wild-type copies correlated with a gradual widening of ISVs (Figures S5D–S5F, S6A–S6C, S6F, and S6G). Nonetheless, *vcl* mutants formed a normal number of tip and stalk cells compared with wild-type embryos (Figures S5A–S5C and S6A–S6E). Furthermore, angiogenesis and anastomosis were completed in *vcla/b* mutant zebrafish (Figures S6A1–S6C1), ISVs were lumenized, and blood flow was established in *vcl* double knockout at 36 hpf (Figures S7A–S7D; Video S7). In addition, no significant differences in heart rate or blood flow velocity between wild-type and *vcl* mutant embryos were observed (Figures S7E and S7F). Overall, these data indicate that *vinculin* deletion results in delayed sprouting angiogenesis; however, functional blood vessels are able to form.

Endothelial vinculin is required and sufficient for the formation of junctional fingers

To assess whether *vinculin* is required for the formation of junctional fingers, we imaged endogenous VE-cadherin in *vinculin* mutants expressing the reporter line *Tg(fli1a:lifeact-EGFP)*. In *vcl* double heterozygotes (*vcla*^{+/−};*vclb*^{+/−}), we observed a significant decrease in both the size and number of the junctional fingers upon lumen opening when compared with wild-type embryos (*vcla*^{+/+};*vclb*^{+/+}; Figures 5D–5E1, 5H, and 5I). Homozygous loss of either *vcla* or *vclb* (*vcla*^{−/−}; *vclb*^{+/−} or *vcla*^{+/−};*vclb*^{−/−}) led to a strong reduction of junctional fingers (Figures 5F, 5F1, 5H, and 5I), an effect that was even more pronounced in *vcl* double mutants (*vcla*^{−/−}; *vclb*^{−/−}; Figures 5G, 5G1, 5H, and 5I). Moreover, we observed gradual differences in the level of junctional finger size and number in the various genotypes corresponding with the number of *vcla/b* mutant alleles (Figures 5H and 5I). Live imaging of *vcl* mutants expressing Pecam1-EGFP (Figures 5J–5L2) confirmed the above observations, as deletion of the *vinculin* paralogs led to a reduction in finger formation in double-heterozygous and in double-knockout mutants (*vcla*^{−/−};*vclb*^{−/−}; Figures 5J–5N).

Figure 3. Alterations in blood flow affect finger size and number

(A–D) Confocal images of representative ISVs from Tg*(kdrl:mCherry-CAAX;fli1a:pecam1a-EGFP)* embryos at 36 hpf before tricaine treatment (A), after treatment with 0.32% tricaine (B), before norepinephrine treatment (C), or after treatment with 60 μM norepinephrine (D). GFP⁺ signal marks Pecam1, and RFP⁺ signal marks the cell membrane. Before pharmacological additions, junctional fingers are evident (A and C, black arrows), and upon tricaine treatment, they regress (B, red arrows), while upon norepinephrine treatment, more fingers are present or they are reinforced (D, black arrows). Scale bar, 10 μm.

(E and F) Line graphs showing the junctional finger size ± SE, finger number ± SE, and lumen diameter ± SE over time after treatment with (E) tricaine or (F) norepinephrine from *Tg(kdrl:mCherry-CAAX;fli1a:pecam1a-EGFP)* embryos (n = 17, E, tricaine; n = 10, F, norepinephrine).

(G) Average finger size per ISV in non-treated or tricaine- or norepinephrine-treated embryos; *p < 0.05 (one-way ANOVA with Dunnett's post-test; n = 11 ISVs from eight embryos).

(H) Number of fingers per ISV in non-treated or tricaine- or norepinephrine-treated embryos; *p < 0.05; ***p < 0.001 (one-way ANOVA with Dunnett's post-test; n = 11 ISVs from eight embryos).
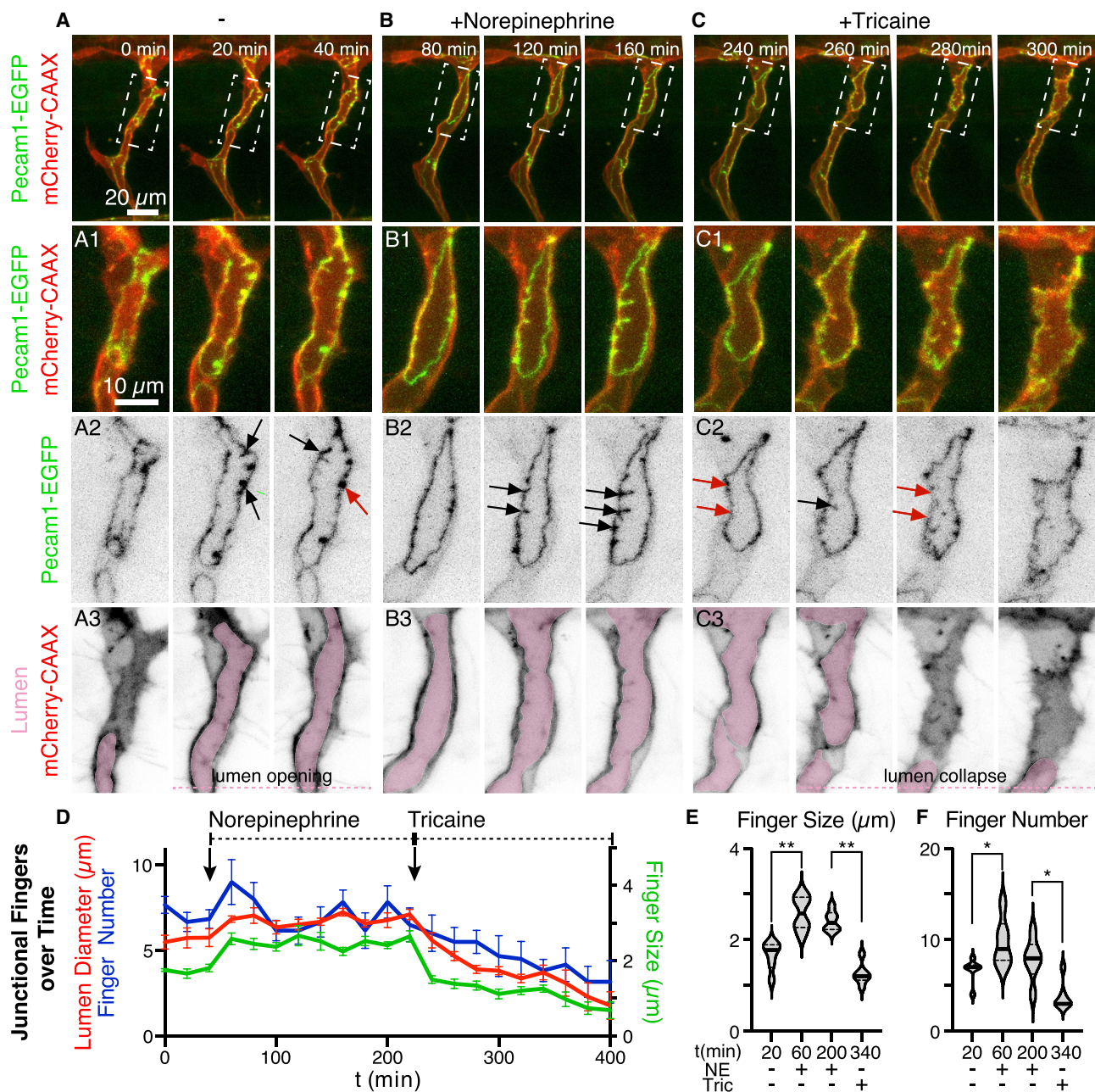
Figure 4. Hemodynamic forces control junctional fingers

(A–C) Stills of time-lapse confocal imaging from a representative 36 hpf Tg(*kdrl:mCherry-CAAX;fli1a:pecam1a-EGFP*) embryo before treatment (A) and after sequential additions of first norepinephrine (B) and then tricaine (C). GFP⁺ signal indicates the junctional marker Pecam-1, and RFP⁺ signal marks the endothelial cell membrane. Scale bar, 20 μm. (A1–C1) Zoom-in images of the outlined boxes in (A)–(C) are shown. Scale bar, 10 μm. (A2–C2) Inverted contrast images of Pecam1-EGFP signal of (A1)–(C1) are shown. (A2) Before lumen opening, no junctional fingers are present; after lumen opening, Pecam1-based junctional fingers assemble (black arrows) and over time undergo regression (red arrows). (B2) Upon norepinephrine treatment, Pecam1 assembles into enlarged junctional fingers (black arrows). (C2) After tricaine treatment, remaining Pecam1-EGFP-positive fingers (black arrows) disappear over time (red arrows). (A3–C3) Inverted contrast images of mCherry-CAAX of (A1)–(C1) are shown. Pink pseudo-colored areas indicate open lumen in the ISV. (B3) After norepinephrine addition, lumen expands. (C3) Treatment with tricaine results in lumen compartmentalization and lumen collapse.

(D) Junctional dynamics analysis of junctional finger size ± SE, finger number ± SE, and lumen diameter ± SE over time before treatment (0–40 min), after treatment with norepinephrine (40–220 min), and after treatment with tricaine (240–400 min) from *Tg(kdrl:mCherry-CAAX;fli1a:pecam1a-EGFP)* embryos (n = 6). (E and F) Average finger size per ISV (E) and number of fingers per ISV (F) at distinct time points before treatments (20 min), after norepinephrine treatment (60 and 220 min), and after tricaine treatment (340 min); *p < 0.05; **p < 0.01 (one-way ANOVA with Dunnett's post-test; n = 6 embryos). See also Figure S3 and Video S2.
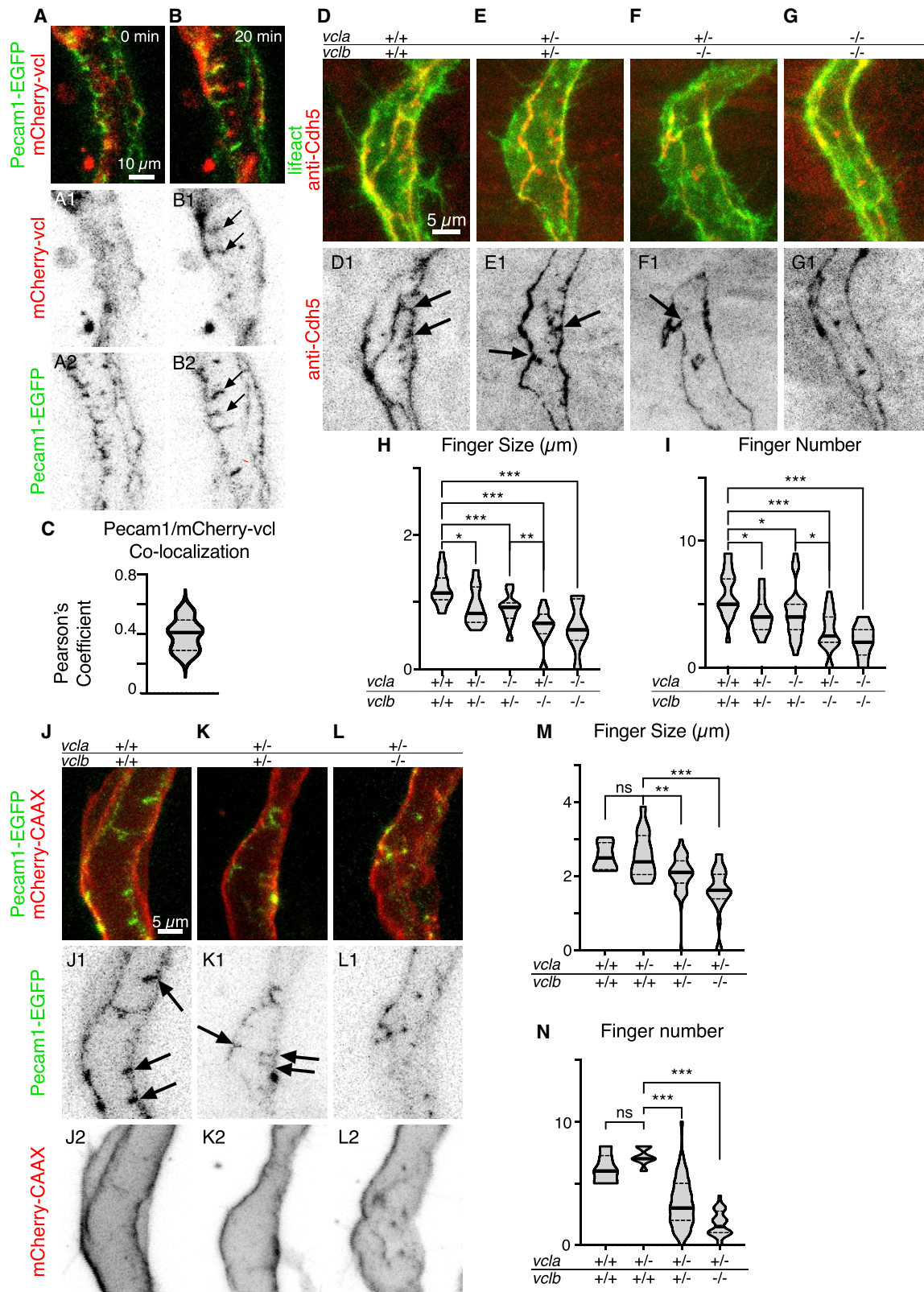
Overall, loss of *vclb* caused stronger defects than mutations *vcla*, indicating a higher requirement for *vclb* than *vcla*. In particular, we observed stronger phenotypes in $vcla^{+/-};vclb^{-/-}$ than in $vcla^{-/-};vclb^{+/-}$ mutants (Figures 5H and 5I). Nevertheless, $vcla^{-/-};vclb^{+/-}$ show stronger phenotypes than double heterozygotes. Thus, both isoforms are involved in ISV formation, with a more pronounced role for *vclb*. Analysis of transcriptome data (Lawson et al., 2020) revealed that *vclb* expression, in contrast to *vcla*, is elevated in endothelial cells compared with non-endothelial cells (Figure S4A). This may account for a slightly stronger mutant phenotype in $vcla^{+/-};vclb^{-/-}$ compared with $vcla^{-/-};vclb^{+/-}$ mutants (Figures 5H and 5I).

Interaction between junctional proteins and the underlying actin cytoskeleton is essential endothelial maintenance and dynamic endothelial cell behaviors (reviewed by Abu Taha and Schnittler, 2014; Phng, 2018). Because vinculin provides a structural link to anchor actin to VE-cadherin, we wanted to test whether changes in the actin cytoskeleton may be responsible for defects in junctional finger formation in *vcl* mutants. However, analysis of Lifeact-EGFP did not reveal any obvious defects in the actin cytoskeleton of *vcl* mutants (Figures 5D–5G and S6H–S6J). We have previously shown that VE-cadherin is required to maintain cortical actin organization during ISV sprouting as well as for junctional elongation during endothelial cell rearrangements (Sauteur et al., 2014). Moreover, junctional elongation also requires actin polymerization (Sauteur et al., 2014). To test the effect of actin polymerization inhibition on finger formation, we treated embryos with latrunculin B (Figures S8A–S8F). We found that a concentration of 0.15 μg/mL, which blocks filopodia formation as well as junction elongation (Phng et al., 2013; Sauteur et al., 2014), or even a higher concentration (0.3 μg/mL) did not perturb the emergence of junctional fingers (Figures S8B, S8C, S8E, and S8F). At higher concentrations (0.6 μg/mL), latrunculin B treatment caused wide-ranging angiogenic defects, such as lumen collapse, junctional instability, and concomitant junctional finger loss (Figures S8D–S8F). Taken together, these data show that actin polymerization does not play a primary role in the formation of junctional fingers.

The above findings demonstrate a strict requirement of vinculin for junctional finger formation. However, these vascular defects may potentially be caused by secondary changes in other tissues in *vcl* mutants. We therefore tested whether endothelial vinculin expression is sufficient to restore junctional finger formation in *vcl* mutants. To this end, we injected plasmid DNA encoding mCherry-vinculin (*kdrl:mCherry-vinculin*) into *vcl* mutant embryos. This resulted in mosaic endothelial-specific expression of vinculin in ISVs (Figures 6A–6D). The expression of mCherry-vinculin did not affect junctional finger formation in injected single-heterozygous embryos ($vcla^{+/-};vclb^{+/+}$; Figures 6A–6A'2), which phenotypically resemble the junctions in wild-type control group (Figures 5M and 5N). In contrast, and consistent with our earlier results, *vcl* double-heterozygous ($vcla^{+/-};vclb^{+/-}$) embryos displayed reduced junctional fingers in mCherry-vinculin-negative ISVs (Figures 6B and 6B1), whereas the ISVs expressing *kdrl:mCherry-vinculin* formed junctional fingers with their neighboring endothelial cells (Figures 6B2–6B'2). Moreover, mCherry-vinculin expression rescued junctional finger formation in homozygous *vclb* mutants ($vcla^{+/-};vclb^{-/-}$), which otherwise did not form junctional fingers at all (Figures 6C–6C'2). Taken together, these results clearly show that vinculin is essential for the formation of junctional fingers and that expression of vinculin within the endothelium is sufficient to promote finger formation in a *vcl*-knockout background.

Increase in blood pressure does not rescue the loss of junctional fingers in vinculin double knockouts

As shown above, the formation of junctional fingers is triggered by an increase in blood pressure. We therefore hypothesized that loss of *vinculin* may reduce the junctional response to hemodynamic forces and that this reduced sensitivity may be overcome by an increase in blood pressure. To test this possibility, we treated *vcl* double-knockout embryos with NE to increase blood pressure at the onset of ISV lumen inflation. Notably, NE treatments did not increase the formation of junctional fingers in *vcl* double-heterozygous ($vcla^{+/-};vclb^{+/-}$) or homozygous ($vcla^{+/-};vclb^{-/-}$) mutants, in contrast to single heterozygotes ($vcla^{+/-};vclb^{+/+}$), in which NE was able to enhance junctional fingers (Figures 6E–6I). Thus, in *vcl* homozygous mutants, endothelial cells appear unresponsive to increased blood pressure. Furthermore, the effect was most pronounced in *vclb* knockouts,

Figure 5. Vinculin is required for the formation of junctional fingers

(A and B) Stills of time-lapse imaging of *Tg(fli1a:pecam1a-EGFP)* embryos at 36 hpf with transient expression of injected *kdrl:mCherry-vinculin (vcl)*. Scale bar, 10 μm. (A1 and B1) Inverted contrast images of mCherry-vcl of (A) and (B) are shown. Black arrows point to co-localization of vinculin and Pecam1. (A2 and B2) Inverted contrast images of Pecam1-EGFP of (A) and (B) are shown. Black arrows point to co-localization of vinculin and Pecam1 at junctional fingers.

(C) Co-localization analysis (Pearson's coefficient, r) of mCherry-vcl signal and Pecam1-EGFP signal at fingers; n = 5 embryos.

(D–G) Images from fixed samples of *Tg(fli1a:lifeact-GFP)* embryos at 36 hpf and immunostained for Cdh5. Scale bar, 5 μm. (D1–G1) Inverted contrast images of anti-Cdh5 of (D)–(G) are shown.

(H and I) Average finger size per ISV (H) and finger number per ISV (I) of wild-type ($vcla^{+/+};vclb^{+/+}$), double-heterozygous ($vcla^{+/-};vclb^{+/-}$), *vcla* homozygous knockout ($vcla^{-/-};vclb^{+/-}$), *vclb* homozygous knockout ($vcla^{+/-};vclb^{-/-}$), or double-knockout ($vcla^{-/-};vclb^{-/-}$) embryos; n = 19 ($vcla^{+/+};vclb^{+/+}$), 11 ($vcla^{+/-};vclb^{+/-}$), 22 ($vcla^{-/-};vclb^{+/-}$), 16 ($vcla^{+/-};vclb^{-/-}$), and 7 ($vcla^{-/-};vclb^{-/-}$) embryos; ns, non-significant; *p < 0.05; **p < 0.01; ***p < 0.001 (one-way ANOVA and Dunnett's post-test).

(J–L) Confocal images of ISVs from live *Tg(kdrl:mCherry-CAAX;fli1a:pecam1a-EGFP)* embryos at 36 hpf of (J) wild-type ($vcla^{+/+};vclb^{+/+}$), (K) double-heterozygous ($vcla^{+/-};vclb^{+/-}$), or (L) *vclb* homozygous ($vcla^{+/-};vclb^{-/-}$). Scale bar, 5 μm. (J1–L1) Inverted contrast images *fli1a:pecam1a-EGFP* of (J)–(L) are shown. (J2–L2) Inverted contrast images of mCherry-CAAX of (J)–(L) are shown. Black arrows indicate junctional fingers; note the absence of junctional fingers in *vclb* homozygous knockouts.

(M and N) Average finger size per ISV (M) and finger number per ISV (N) of wild-type ($vcla^{+/+};vclb^{+/+}$), single-heterozygous ($vcla^{+/-};vclb^{+/+}$), double-heterozygous ($vcla^{+/-};vclb^{+/-}$), or *vclb* homozygous knockout ($vcla^{+/-};vclb^{-/-}$) embryos; n = 4 ($vcla^{+/+};vclb^{+/+}$), 9 ($vcla^{+/-};vclb^{+/+}$), 22 ($vcla^{+/-};vclb^{+/-}$), and 12 ($vcla^{+/-};vclb^{-/-}$) embryos; **p < 0.01; ***p < 0.001 (one-way ANOVA and Dunnett's post-test).

See also Videos S3 and S4.
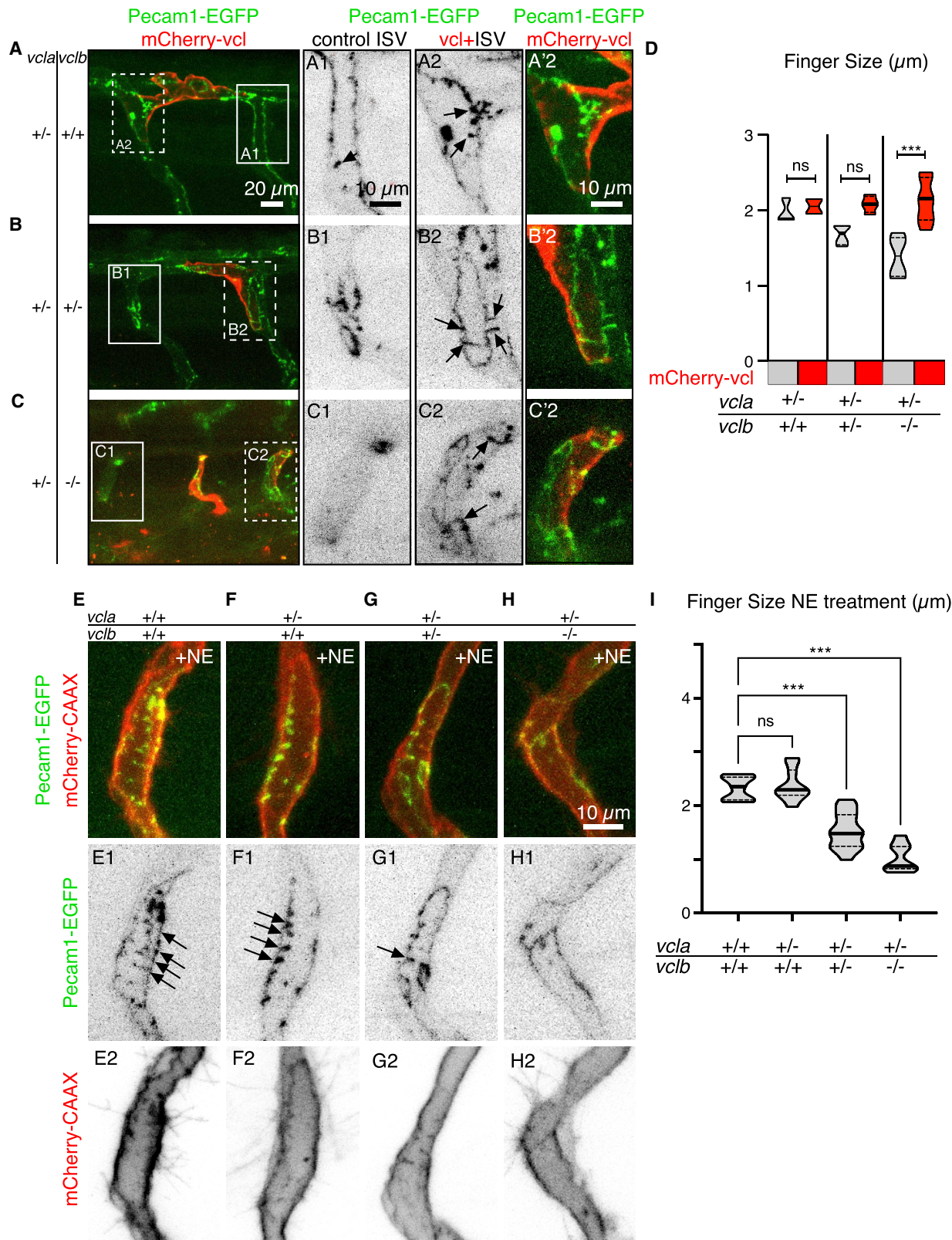
whereas combinations of mutant and wild-type alleles displayed an intermediate phenotype (Figure 6I), supporting the notion of a dose-dependent requirement of vinculin in this process. Taken together, these results point to a mechanism in which vinculin recruitment acts as an adaptive response to elevated junctional tension during angiogenic sprouting.

DISCUSSION

Dynamic junctional remodeling is essential for blood vessel formation, maintenance, and function. Here, we describe the formation of junctional fingers as a novel trait of junctional remodeling that occurs during lumen formation of developing ISVs in the zebrafish embryo. Junctional fingers appear as junctional folds of up to 3 to 4 μm, which are oriented perpendicular to the originating junction and show a characteristic dynamic behavior. Junctional fingers are formed upon the interconnection between the dorsal aorta and the sprouting ISV, which triggers exposure of sprouting endothelial cells to luminal pressure. However, junctional fingers disappear once ISVs have achieved patency and blood flow is firmly established. This specific response to blood pressure renders junctional fingers as a novel *in vivo* paradigm for the study of junctional dynamics in response to extrinsic forces.

Our studies demonstrate that formation of junctional fingers relies on the recruitment of vinculin and thus point to an interconnection between junctional tension, junctional remodeling, and blood vessel morphogenesis. Recent studies have established distinct roles for *vcla* and *vclb* during zebrafish heart development, which reflect their expression in the myocardium and epicardium, respectively (Cheng et al., 2016; Fukuda et al., 2019; Han et al., 2017). In contrast, *vcla* and *vclb* are both expressed in the zebrafish endothelium (Lawson et al., 2020), with *vclb* being slightly higher expressed in endothelial cells than *vcla* (Figure S4A; Lawson et al., 2020). Correspondingly, we notice phenotypic variation in different mutant allele combinations (e.g., *vcla*$^{-/-}$;*vclb*$^{+/-}$ versus *vcla*$^{+/-}$;*vclb*$^{-/-}$), showing a higher requirement for *vclb* than *vcla*. Nevertheless, different genotypes display different phenotypic strength during ISV sprouting and junctional finger formation, largely depending on the number of *vcla/b* mutant alleles present. This indicates that

the two proteins have redundant functions during blood vessel formation and that their requirement is highly dose dependent.

Dynamic changes in junctional organization have been studied previously in different contexts. In particular, perpendicular-oriented endothelial cell-cell junctions have been described as serrated junctions, discontinuous junctions, focal adherens junctions (FAJs), and VE-cadherin fingers (Bentley et al., 2014; Hayer et al., 2016; Huveneers et al., 2012). Serrated and discontinuous junctions have been associated with active or remodeling junctions (Bentley et al., 2014). The junctional fingers we describe here appear as invaginations of stable and continuous junctions and are morphologically similar to VE-cadherin fingers and FAJs that have been previously described in HUVECs (Huveneers et al., 2012; Dorland and Huveneers, 2016; Hayer et al., 2016). However, because of the presence of Pecam1 and other junctional components (ZO1, VE-cadherin, and F-actin), we call them "junctional fingers" rather than "VE-cadherin fingers" in the current study.

VE-cadherin fingers and FAJs are involved in mechanical coupling between endothelial cells and are controlled by actomyosin contractility (Huveneers et al., 2012; Dorland and Huveneers, 2016; Hayer et al., 2016). In agreement with this, junctional fingers form when endothelial sprouts encounter blood pressure. Modulation of blood flow by pharmacological intervention leads to a graded response, with more and longer junctional fingers correlating with higher blood pressure, suggesting that junctional fingers are an adaptive response of endothelial cells to increased mechanical stress. In fact, the specific localization of vinculin to junctional fingers indicates that they are experiencing elevated junctional tension on the VE-cadherin-catenin complex. Our genetic analyses show that vinculin is required for the formation of junctional fingers and mosaic expression in sprouting endothelial cells can rescue defects arising from partial *vinculin* loss of function or complete *vinculin* knockout. Our previous cell culture experiments have shown that tension-induced vinculin localization to FAJs protects these junctions against mechanical stress (Huveneers et al., 2012). Our *in vivo* observations suggest that vinculin may have a dual role during vascular lumen inflation. First, a local increase in junctional tension triggers recruitment of vinculin to the endothelial junction, which subsequently leads to the formation of junctional fingers. Alternatively, vinculin may become localized

Figure 6. Increase in blood pressure does not rescue the loss of junctional fingers in *vinculin* mutants

(A–C) Confocal images of 36 hpf Tg(*fli1a:pecam1a-EGFP*) embryos injected with *kdrl:mCherry-vinculin* with genotypes (A) single-heterozygous mutant (*vcla*$^{+/-}$;*vclb*$^{+/+}$), (B) double-heterozygous mutant (*vcla*$^{+/-}$;*vclb*$^{+/-}$), or (C) *vclb* homozygous mutant (*vcla*$^{+/-}$;*vclb*$^{-/-}$). Scale bar, 20 μm. (A1–C1) Zoom-in inverted contrast images of *fli1a:pecam1a-EGFP* of the insets in (A)–(C) of an ISV without *kdrl:mCherry-vinculin* expression (internal control) are shown. Scale bar, 10 μm. (A2–C2) Zoom-in inverted contrast images of *fli1a:pecam1a-EGFP* of the insets in (A)–(C) of an *kdrl:mCherry-vinculin* expressing ISV are shown. (A'2–C'2) Merged image of (A2)–(C2) is shown. Arrows indicate junctional fingers.

(D) Average finger size per ISV ± SE of *vinculin* single-heterozygous mutant (*vcla*$^{+/-}$;*vclb*$^{+/+}$), double-heterozygous mutant (*vcla*$^{+/-}$;*vclb*$^{+/-}$), or *vclb* homozygous mutant (*vcla*$^{+/-}$;*vclb*$^{-/-}$) embryos with or without *kdrl:mCherry-vinculin* expression (n = 2 [*vcla*$^{+/-}$;*vclb*$^{+/+}$], 3 [*vcla*$^{+/-}$;*vclb*$^{+/-}$], and 5 [*vcla*$^{+/-}$;*vclb*$^{-/-}$] embryos); ***p < 0.001 (one-way ANOVA with Dunnett's post-test).

(E–H) Confocal images of ISVs from *Tg(kdrl:mCherry-CAAX;fli1a:pecam1a-EGFP)* embryos at 36 hpf with genotypes (E) wild-type (*vcla*$^{+/+}$;*vclb*$^{+/+}$), (F) single-heterozygous mutant (*vcla*$^{+/-}$;*vclb*$^{+/+}$), (G) double-heterozygous mutant (*vcla*$^{+/-}$;*vclb*$^{+/-}$), or (H) *vclb* homozygous mutant (*vcla*$^{+/-}$;*vclb*$^{-/-}$) after treatment with 60 μM norepinephrine (NE). GFP$^+$ signal marks Pecam-1, and RFP$^+$ signal indicates the cell membrane. Scale bar, 10 μm. (E1–H1) Inverted contrast images of Pecam1-EGFP of the outlined boxes in (E) are shown. Black arrows indicate junctional fingers. Note the absence of junctional fingers in *vclb* homozygous knockouts. (E2–H2) Inverted contrast images of mCherry-CAAX of the outlined boxes in (E)–(H) are shown.

(I) Average finger size per ISV after NE treatment of the genotypes wild-type (*vcla*$^{+/+}$;*vclb*$^{+/+}$), single-heterozygous mutant (*vcla*$^{+/-}$;*vclb*$^{+/+}$), double-heterozygous mutant (*vcla*$^{+/-}$;*vclb*$^{+/-}$), or *vclb* homozygous mutant (*vcla*$^{+/-}$;*vclb*$^{-/-}$; n = 7 [*vcla*$^{+/+}$;*vclb*$^{+/+}$], 10 [*vcla*$^{+/-}$;*vcla*$^{+/+}$], 17 [*vcla*$^{+/-}$;*vclb*$^{+/-}$], and 7 [*vcla*$^{+/-}$;*vclb*$^{-/-}$] ISVs); ***p < 0.001 (one-way ANOVA with Dunnett's post-test).
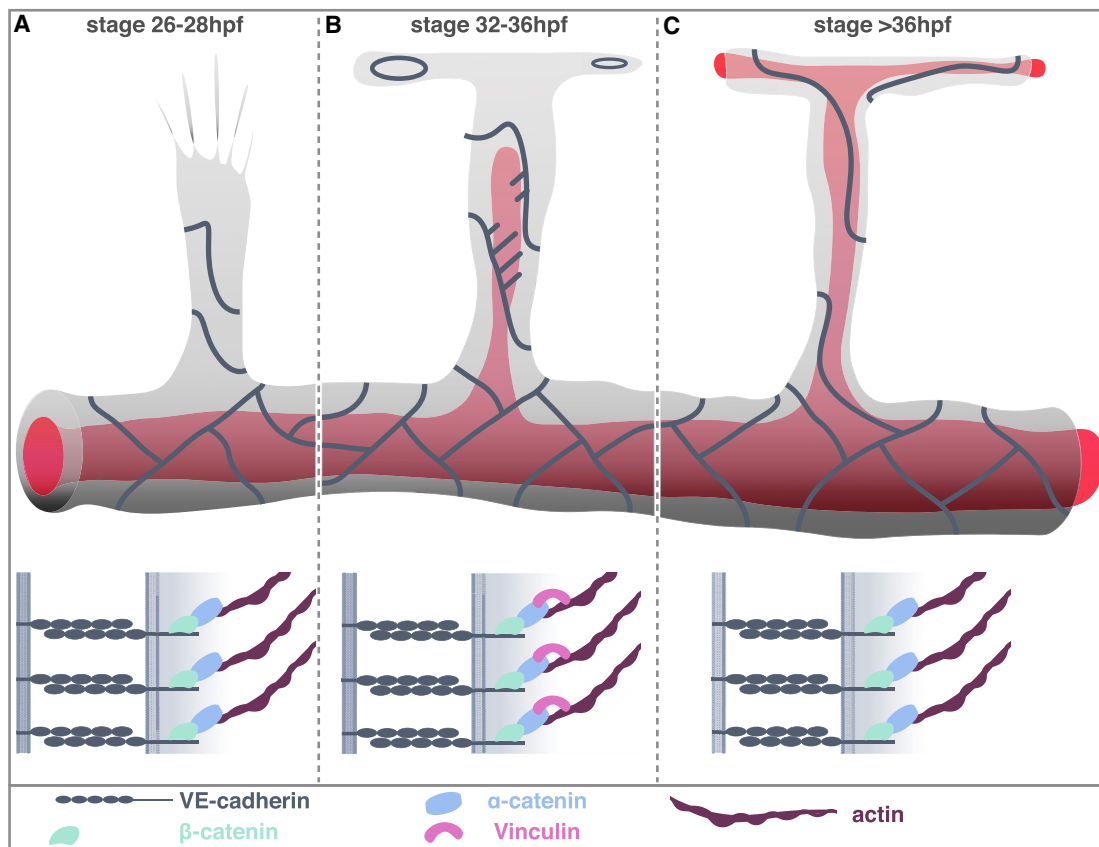
Figure 7. Summary model

(A and B) During ISV sprouting (A; 26–28 hpf), endothelial cell junctions appear straight. Cell rearrangement leads to a multicellular configuration. Lumen expansion (B; 32–36 hpf) is shown. Once the lumen is opened, endothelial cells in the nascent sprout become exposed to blood pressure. Junctional fingers occur in regions facing the expanding lumen. Vinculin is localized at junctional fingers. At this stage, the ISV is not yet patent.

(C) Commencement of blood flow (40 hpf). Anastomosis generates a continuous vascular lumen permitting blood flow, resulting in the disappearance of junctional fingers, and junctional vinculin is not detectable anymore.

upon junctional finger formation. In agreement with our study, recruitment of vinculin-a to myocardial cell-cell junctions depends on the mechanical force generated by myocardial contractility (Fukuda et al., 2019). Here, vinculin recruits actin regulators and promotes myofiber maturation. It will be of interest to discern the molecular pathways that regulate vinculin recruitment and function during vascular lumen expansion. It has recently been shown that vinculin is essential for angiogenesis in the postnatal mouse retina and that loss of vinculin leads to increased blood vessel regression downstream of non-canonical Wnt signaling (Carvalho et al., 2019). In this context, shear stress promotes VE-cadherin localization of vinculin in a Wnt5a-dependent manner. In contrast to vessel regression, which is regulated by blood-flow-mediated shear stress (reviewed by Korn and Augustin, 2015), initial lumen expansion in the ISV is driven by blood pressure, which induces circumferential stretch (reviewed by Hoefer et al., 2013). Therefore, hemodynamic forces, shear stress and circumferential stretch, promote localization of vinculin to endothelial cell-cell junctions.

Junctional fingers show a dynamic behavior. They form during lumen expansion in sprouting vessels but regress once blood flow is established. A likely scenario to explain these findings is that lumen inflation increases junctional tension, which is subsequently relieved by the commencement of blood flow. Further studies will be required to discern whether shear stress influences junctional finger maintenance or regression. However, we did not detect junctional fingers in the dorsal aorta or the posterior cardinal vein. These blood vessels are formed by vasculogenesis, which is likely to preclude junctional finger formation because of different hemodynamic conditions.

During vascular morphogenesis as well as in functional blood vessels, endothelial cells generate dynamic junctional protrusions, called junction-based lamellipodia (JBL) or junction-associated intermittent lamellipodia (JAIL), which have been observed in different vascular beds of zebrafish embryo as well as mouse embryos and the postnatal retina (reviewed by Cao and Schnittler, 2019; Fonseca et al., 2020). Live imaging of JBL showed that they are highly dynamic oscillatory structures and are associated with cell movements within the endothelium in zebrafish embryos (Paatero et al., 2018; reviewed by Okuda and Hogan, 2020). Thus, JBL form in regions of high junctional turnover and reduced junctional stability. In contrast, the junctional

fingers we describe here are transient but do not oscillate. Their dynamic behavior and association with vinculin indicate that they are strengthened junctions, which support junctional stability to maintain blood vessel integrity in response to sudden changes in extrinsic forces.

In conclusion, our results support a model (Figure 7) in which endothelial cell-cell junctions form finger-like invaginations during vascular lumen expansion in response to junctional stretch induced by an increase of blood pressure. Junctional fingers recruit vinculin and rely on it for their formation and stabilization. Taken together, junctional fingers represent a novel paradigm to study endothelial cell dynamics and junctional remodeling in response to mechanical forces during blood vessel morphogenesis *in vivo*.

STAR★METHODS

Detailed methods are provided in the online version of this paper and include the following:

- KEY RESOURCES TABLE
- RESOURCE AVAILABILITY
  - Lead contact
  - Materials availability
  - Data and code availability
- EXPERIMENTAL MODEL AND SUBJECT DETAILS
  - Zebrafish lines and maintenance
- METHOD DETAILS
  - Genotyping of the vcl mutant lines
  - Generation of kdrl:mCherry-vinculin expression plasmid
  - Embryo microinjections
  - Immunofluorescence
  - Pharmacological treatments
  - Imaging and image analysis
- QUANTIFICATION AND STATISTICAL ANALYSIS

SUPPLEMENTAL INFORMATION

Supplemental information can be found online at https://doi.org/10.1016/j.celrep.2022.110658.

AUTHOR CONTRIBUTIONS

H.-G.B. and S.H. conceived the idea and directed the work. M.A. provided supervision and financial support. M.P.K. and M.M.v.d.S. designed and performed experiments. J.Y. performed experiments. H.-G.B., S.H., M.A., M.P.K., and M.M.v.d.S. analyzed the data. M.K.H., B.K., and J.d.R. provided essential reagents. M.P.K. and M.M.v.d.S. prepared figures. H.-G.B., S.H., M.P.K., and M.M.v.d.S. wrote the manuscript. All authors reviewed the manuscript.

REFERENCES

Abu Taha, A., and Schnittler, H.-J. (2014). Dynamics between actin and the VE-cadherin/catenin complex. Cell Adhes. Migration *8*, 125–135. https://doi.org/10.4161/cam.28243.

Aleström, P., D'Angelo, L., Midtlyng, P.J., Schorderet, D.F., Schulte-Merker, S., Sohm, F., and Warner, S. (2019). Zebrafish: housing and husbandry recommendations. Lab Anim. *51*, 213–214. https://doi.org/10.1177/0023677219869037.

Ando, K., Fukuhara, S., Izumi, N., Nakajima, H., Fukui, H., Kelsh, R.N., and Mochizuki, N. (2016). Clarification of mural cell coverage of vascular endothelial cells by live imaging of zebrafish. Development *143*, 1328–1339. https://doi.org/10.1242/dev.132654.

Angulo-Urarte, A., van der Wal, T., and Huveneers, S. (2020). Cell-cell junctions as sensors and transducers of mechanical forces. BBA Biomembranes *1862*, 183316. https://doi.org/10.1016/j.bbamem.2020.183316.

Baeyens, N., and Schwartz, M.A. (2016). Biomechanics of vascular mechanosensation and remodeling. MBoC *27*, 7–11. https://doi.org/10.1091/mbc.E14-11-1522.

Balciunas, D., Wangensteen, K.J., Wilber, A., Bell, J., Geurts, A., Sivasubbu, S., Wang, X., Hackett, P.B., Largaespada, D.A., McIvor, R.S., and Ekker, S.C. (2006). Harnessing a high cargo-capacity transposon for genetic applications in vertebrates. Plos Genet. *2*, e169. https://doi.org/10.1371/journal.pgen.0020169.

Barry, A.K., Wang, N., and Leckband, D.E. (2015). Local VE-cadherin mechanotransduction triggers long-ranged remodeling of endothelial monolayers. J. Cell Sci. *128*, 1341–1351. https://doi.org/10.1242/jcs.159954.

Bentley, K., Franco, C.A., Philippides, A., Blanco, R., Dierkes, M., Gebala, V., Stanchi, F., Jones, M., Aspalter, I.M., Cagna, G., et al. (2014). The role of differential VE-cadherin dynamics in cell rearrangement during angiogenesis. Nat. Cell Biol. *16*, 309–321. https://doi.org/10.1038/ncb2926.

Betz, C., Lenard, A., Belting, H.-G., and Affolter, M. (2016). Cell behaviors and dynamics during angiogenesis. Development *143*, 2249–2260. https://doi.org/10.1242/dev.135616.

Blum, Y., Belting, H.-G., Ellertsdottir, E., Herwig, L., Lüders, F., and Affolter, M. (2008). Complex cell rearrangements during intersegmental vessel sprouting and vessel fusion in the zebrafish embryo. Dev. Biol. *316*, 312–322. https://doi.org/10.1016/j.ydbio.2008.01.038.

Bolte, S., and Cordelières, F.P. (2006). A guided tour into subcellular colocalization analysis in light microscopy. J. Microsc. *224*, 213–232. https://doi.org/10.1111/j.1365-2818.2006.01706.x.

Burkel, B.M., Dassow, von, G., and Bement, W.M. (2007). Versatile fluorescent probes for actin filaments based on the actin-binding domain of utrophin. Cell Motil. Cytoskeleton *64*, 822–832. https://doi.org/10.1002/cm.20226.

Cao, J., and Schnittler, H. (2019). Putting VE-cadherin into JAIL for junction remodeling. J. Cell Sci. *132*, jcs222893–19. https://doi.org/10.1242/jcs.222893.

Carvalho, J.R., Fortunato, I.C., Fonseca, C.G., Pezzarossa, A., Barbacena, P., Dominguez-Cejudo, M.A., Vasconcelos, F.F., Santos, N.C., Carvalho, F.A., and Franco, C.A. (2019). Non-canonical Wnt signaling regulates junctional mechanocoupling during angiogenic collective cell migration. eLife *8*. https://doi.org/10.7554/eLife.45853.

Chen, Q., Jiang, L., Li, C., Hu, D., Bu, J.-W., Cai, D., and Du, J.-L. (2012). Haemodynamics-driven developmental pruning of brain vasculature in zebrafish. Plos Biol. *10*, e1001374–18. https://doi.org/10.1371/journal.pbio.1001374.

Cheng, F., Miao, L., Wu, Q., Gong, X., Xiong, J., and Zhang, J. (2016). Vinculin b deficiency causes epicardial hyperplasia and coronary vessel disorganization in zebrafish. Development *143*, 3522–3531. https://doi.org/10.1242/dev.132936.

Conway, D.E., Breckenridge, M.T., Hinde, E., Gratton, E., Chen, C.S., and Schwartz, M.A. (2013). Fluid shear stress on endothelial cells modulates mechanical tension across VE-cadherin and PECAM-1. Curr. Biol. *23*, 1024–1030. https://doi.org/10.1016/j.cub.2013.04.049.

De Luca, E., Zaccaria, G.M., Hadhoud, M., Rizzo, G., Ponzini, R., Morbiducci, U., and Santoro, M.M. (2014). ZebraBeat: a flexible platform for the analysis of the cardiac rate in zebrafish embryos. Sci. Rep. *4*, 835–913. https://doi.org/10.1038/srep04898.

Dorland, Y.L., and Huveneers, S. (2016). Cell–cell junctional mechanotransduction in endothelial remodeling. Cell Mol. Life Sci., 1–14. https://doi.org/10.1007/s00018-016-2325-8.

Duchemin, A.-L., Vignes, H., Vermot, J., and Chow, R. (2019). Mechanotransduction in cardiovascular morphogenesis and tissue engineering. Curr. Opin. Genet. Dev. *57*, 106–116. https://doi.org/10.1016/j.gde.2019.08.002.

El-Brolosy, M.A., Kontarakis, Z., Rossi, A., Kuenne, C., nther, S.G.X., Fukuda, N., Kikhi, K., Boezio, G.L.M., Takacs, C.M., Lai, S.-L., et al. (2019). Genetic compensation triggered by mutant mRNA degradation. Nat. Publishing Group, 1–26. https://doi.org/10.1038/s41586-019-1064-z.

Fonseca, C.G., Barbacena, P., and Franco, C.A. (2020). Endothelial cells on the move: dynamics in vascular morphogenesis and disease. Vasc. Biol. *2*, H29–H43. https://doi.org/10.1530/VB-20-0007.

Fukuda, R., Gunawan, F., Ramadass, R., Beisaw, A., Konzer, A., Mullapudi, S.T., Gentile, A., Maischein, H.-M., Graumann, J., and Stainier, D.Y.R. (2019). Mechanical forces regulate cardiomyocyte myofilament maturation via the VCL-SSH1-CFL Axis. Dev. Cell *51*, 62–77.e5. https://doi.org/10.1016/j.devcel.2019.08.006.

Gebala, V., Collins, R., Geudens, I., Phng, L.-K., and Gerhardt, H. (2016). Blood flow drives lumen formation by inverse membrane blebbing during angiogenesis in vivo. Nat. Cell Biol. *18*, 443–450. https://doi.org/10.1038/ncb3320.

Han, M.K.L., van der Krogt, G.N.M., and de Rooij, J. (2017). Zygotic vinculin is not essential for embryonic development in zebrafish. PLoS ONE *12*, e0182278. https://doi.org/10.1371/journal.pone.0182278.

Hayer, A., Shao, L., Chung, M., Joubert, L.-M., Yang, H.W., Tsai, F.-C., Bisaria, A., Betzig, E., and Meyer, T. (2016). Engulfed cadherin fingers are polarized junctional structures between collectively migrating endothelial cells. Nat. Cell Biol. *18*, 1311–1323. https://doi.org/10.1038/ncb3438.

Herwig, L., Blum, Y., Krudewig, A., Ellertsdottir, E., Lenard, A., Belting, H.-G., and Affolter, M. (2011). Distinct cellular mechanisms of blood vessel fusion in the zebrafish embryo. Curr. Biol. *21*, 1942–1948. https://doi.org/10.1016/j.cub.2011.10.016.

Hoefer, I.E., Adel, den, B., and Daemen, M.J.A.P. (2013). Biomechanical factors as triggers of vascular growth. Cardiovasc. Res. *99*, 276–283. https://doi.org/10.1093/cvr/cvt089.

Hogan, B.M., Bos, F.L., Bussmann, J., Witte, M., Chi, N.C., Duckers, H.J., and Schulte-Merker, S. (2009). ccbe1 is required for embryonic lymphangiogenesis and venous sprouting. Nat. Genet. *41*, 396–398. https://doi.org/10.1038/ng.321.

Hogan, B.M., and Schulte-Merker, S. (2017). How to plumb a pisces: understanding vascular development and disease using zebrafish embryos. DEVCEL *42*, 567–583. https://doi.org/10.1016/j.devcel.2017.08.015.

Huveneers, S., Oldenburg, J., Spanjaard, E., van der Krogt, G., Grigoriev, I., Akhmanova, A., Rehmann, H., and de Rooij, J. (2012). Vinculin associates with endothelial VE-cadherin junctions to control force-dependent remodeling. J. Cell Biol. *196*, 641–652. https://doi.org/10.1083/jcb.201108120.

Komarova, Y.A., Kruse, K., Mehta, D., and Malik, A.B. (2017). Protein interactions at endothelial junctions and signaling mechanisms regulating endothelial permeability. Circ. Res. *120*, 179–206. https://doi.org/10.1161/CIRCRESAHA.116.306534.

Korn, C., and Augustin, H.G. (2015). Mechanisms of vessel pruning and regression. DEVCEL *34*, 5–17. https://doi.org/10.1016/j.devcel.2015.06.004.

Lagendijk, A.K., Gomez, G.A., Baek, S., Hesselson, D., Hughes, W.E., Paterson, S., Conway, D.E., Belting, H.-G., Affolter, M., Smith, K.A., et al. (2017). Live imaging molecular changes in junctional tension upon VE-cadherin in zebrafish. Nat. Commun., 1–12. https://doi.org/10.1038/s41467-017-01325-6.

Lampugnani, M.G., Dejana, E., and Giampietro, C. (2017). Vascular endothelial (VE)-Cadherin, endothelial adherens junctions, and vascular disease (2017). Cold Spring Harbor Perspect. Biol. *9*. https://doi.org/10.1101/cshperspect.a033720.

Lawson, N.D., Li, R., Shin, M., Grosse, A., Yukselen, O., Stone, O.A., Kucukural, A., and Zhu, L. (2020). An improved zebrafish transcriptome annotation for sensitive and comprehensive detection of cell type-specific genes. eLife *9*, 347–428. https://doi.org/10.7554/eLife.55792.

Lawson, N.D., and Weinstein, B.M. (2002). In vivo imaging of embryonic vascular development using transgenic zebrafish. Dev. Biol. *248*, 307–318. https://doi.org/10.1006/dbio.2002.0711.

Lenard, A., Ellertsdottir, E., Herwig, L., Krudewig, A., Sauteur, L., Belting, H.-G., and Affolter, M. (2013). In vivo analysis reveals a highly stereotypic morphogenetic pathway of vascular anastomosis. Dev. Cell *25*, 492–506. https://doi.org/10.1016/j.devcel.2013.05.010.

Liu, Z., Tan, J.L., Cohen, D.M., Yang, M.T., Sniadecki, N.J., Ruiz, S.A., Nelson, C.M., and Chen, C.S. (2010). Mechanical tugging force regulates the size of cell-cell junctions. Proc. Natl. Acad. Sci. U S A. *107*, 9944–9949. https://doi.org/10.1073/pnas.0914547107.

Meeker, N.D., Hutchinson, S.A., Ho, L., and Trede, N.S. (2007). Method for isolation of PCR-ready genomic DNA from zebrafish tissues. Biotechniques *43*, 610–614. https://doi.org/10.2144/000112619.

Okuda, K.S., and Hogan, B.M. (2020). Endothelial cell dynamics in vascular development: insights from live-imaging in zebrafish. Front Physiol. *11*, 842. https://doi.org/10.3389/fphys.2020.00842.

Paatero, I., Sauteur, L., Lee, M., Lagendijk, A.K., Heutschi, D., Wiesner, C., Guzmán, C., Bieli, D., Hogan, B.M., Affolter, M., and Belting, H.-G. (2018). Junction-based lamellipodia drive endothelial cell rearrangements in vivo via a VE-cadherin-F-actin based oscillatory cell-cell interaction. Nat. Commun., 1–13. https://doi.org/10.1038/s41467-018-05851-9.

Phng, L.-K. (2018). Endothelial cell dynamics during blood vessel morphogenesis. In Zebrafish, Medaka, and Other Small Fishes, New Model Animals in Biology, Medicine, and beyond (Singapore: Springer Singapore), pp. 17–35. https://doi.org/10.1007/978-981-13-1879-5_2.

Phng, L.-K., and Belting, H.-G. (2021). Endothelial cell mechanics and blood flow forces in vascular morphogenesis. Semin. Cell Dev. Biol., 1–12. https://doi.org/10.1016/j.semcdb.2021.06.005.

Phng, L.-K., Stanchi, F., and Gerhardt, H. (2013). Filopodia are dispensable for endothelial tip cell guidance. Development *140*, 4031–4040. https://doi.org/10.1242/dev.097352.

Potente, M., Gerhardt, H., and Carmeliet, P. (2011). Basic and therapeutic aspects of angiogenesis. Cell *146*, 873–887. https://doi.org/10.1016/j.cell.2011.08.039.

Roman, B.L., and Pekkan, K. (2012). Mechanotransduction in embryonic vascular development. Biomech. Model Mechanobiol. *11*, 1149–1168. https://doi.org/10.1007/s10237-012-0412-9.

Sauteur, L., Krudewig, A., Herwig, L., Ehrenfeuchter, N., Lenard, A., Affolter, M., and Belting, H.-G. (2014). Cdh5/VE-cadherin promotes endothelial cell interface elongation via cortical actin polymerization during angiogenic sprouting. CellReports *9*, 504–513. https://doi.org/10.1016/j.celrep.2014.09.024.

Szymborska, A., and Gerhardt, H. (2018). Hold me, but not too tight—endothelial cell–cell junctions in angiogenesis. Cold Spring Harbor Perspect. Biol. *10*, a029223-17. https://doi.org/10.1101/cshperspect.a029223.

Traver, D., Paw, B.H., Poss, K.D., Penberthy, W.T., Lin, S., and Zon, L.I. (2003). Transplantation and in vivo imaging of multilineage engraftment in zebrafish

bloodless mutants. Nat. Immunol. *4*, 1238–1246. https://doi.org/10.1038/ni1007.

Twiss, F., le Duc, Q., Van Der Horst, S., Tabdili, H., van der Krogt, G., Wang, N., Rehmann, H., Huveneers, S., Leckband, D.E., and de Rooij, J. (2012). Vinculin-dependent Cadherin mechanosensing regulates efficient epithelial barrier formation. Biol. Open *1*, 1128–1140. https://doi.org/10.1242/bio.20122428.

Tzima, E., Irani-Tehrani, M., Kiosses, W.B., Dejana, E., Schultz, D.A., Engel-hardt, B., Cao, G., DeLisser, H., and Schwartz, M.A. (2005). A mechanosen-sory complex that mediates the endothelial cell response to fluid shear stress. Nature *437*, 426–431. https://doi.org/10.1038/nature03952.

Wallez, Y., and Huber, P. (2008). Endothelial adherens and tight junctions in vascular homeostasis, inflammation and angiogenesis. Biochim. Biophys. Acta (Bba) Biomembranes *1778*, 794–809. https://doi.org/10.1016/j.bba-mem.2007.09.003.

Yao, M., Qiu, W., Liu, R., Efremov, A.K., Cong, P., Seddiki, R., Payre, M., Lim, C.T., Ladoux, B., ge, R.E.M.M.E., and Yan, J. (2014). Force-dependent confor-mational switch of α-catenin controls vinculin binding. Nat. Commun., 1–12. https://doi.org/10.1038/ncomms5525.

STAR★METHODS

KEY RESOURCES TABLE

REAGENT or RESOURCE	SOURCE	IDENTIFIER
Antibodies		
Mouse monoclonal anti-human-ZO-1	Thermo Fisher Scientific	CAT# 33-9100; RRID: AB_87181
Guinea pig-anti-zebrafish-VE-cadherin	Paatero et al. (2018)	N/A
Mouse monoclonal anti-vinculin (hVIN-1 clone)	Sigma-Aldrich	CAT# V9131; RRID:AB_477629
Alexa Fluor 405 goat anti-mouse IgG	Thermo Fisher Scientific	CAT# A-31553; RRID:AB_221604
Alexa Fluor 568 goat anti-guinea pig IgG	Thermo Fisher Scientific	CAT# A-11075; RRID:AB_2534119
Alexa Fluor 405 goat anti-rabbit pig IgG	Thermo Fisher Scientific	CAT# A-31556; RRID:AB_221605
Chemicals, peptides, and recombinant proteins		
Pierce Immunostain Enhancer medium	Thermo Fisher Scientific	CAT# 46644
Methylene Blue	Sigma-Aldrich	CAT#1.15943
Tricaine	Sigma-Aldrich	CAT# A5040
Norepinephrine	Sigma-Aldrich	CAT# A7257
Latrunculin B	Sigma-Aldrich	CAT# L5288
Proteinase K	Roche	CAT# 3115836001
OneTaq DNA polymerase	NEB	CAT# M0480
Paraformaldehyde	Merck	CAT# 30525-89-4
Triton X-100	Sigma-Aldrich	CAT# 9036-19-5
Bovine Serum Albumin	Roche	CAT# 10735086001
Sodium azide	Sigma-Aldrich	CAT# S2002
1-phenyl-2-thiourea (PTU)	Sigma-Aldrich	CAT# P7629
Low gelling temperature agarose	Sigma-Aldrich	CAT# A9414
Experimental models: Organisms/strains		
Zebrafish vcla^{hu10818};vclb^{hu11202}	Han et al., 2017	ZDB-FISH-180619-2
Tg(fli1a:EGFP)^{y1}	Lawson and Weinstein, 2002	ZDB-ALT-011017-8
Tg(gata1a:DsRed)^{sd2}	Traver et al., 2003	ZDB-ALT-051223-6
Tg(fli1a:pecam1a-EGFP)^{ncv27}	Ando et al., 2016	ZDB-ALT-160609-6
Tg(fli1a:GFF)^{ubs3}	Herwig et al., 2011	ZDB-ALT-120113-6
Tg(UAS:EGFP-hZO1)^{ubs5}	Herwig et al., 2011	ZDB-ALT-120113-7
Tg(UAS:mRuby2-UCHD)^{ubs20}	Paatero et al., 2018	ZDB-ALT-190628-2
Tg(kdrl:EGFP-nls)^{ubs1}	Blum et al., 2008	ZDB-ALT-081105-1
Tg(kdrl:mCherry-CAAX)^{s916}	Hogan et al., 2009	ZDB-ALT-090506-2
Tg(fli1a:Lifeact-EGFP)^{zf495Tg}	Phng et al., 2013	ZDB-ALT-140610-8
TgBAC(ve-cad:ve-cadTS)^{uq11bh}	Lagendijk et al., 2017	ZDB-ALT-181106-3
Oligonucleotides		
vcla – Forward primer: AGCTGATGATCTGAATC AGGTGTG	This paper	N/A
vcla – Reverse primer: TCGTTCAATCACTCGTG CAAACAG	This paper	N/A
vcla – Forward wt: ACCATGGAGGACTTGATCACT	This paper	N/A
vcla – Reverse –mutant: GGTCCCAGGTTTTTAG TGTAAGT	This paper	N/A
vclb – Forward primer: CGGTAGTTAGTTAGTTGT AGAGGGAGTC	This paper	N/A
vclb – Reverse primer: AATGAGAAAGCCTGAAT GTGCG	This paper	N/A

(Continued on next page)

Continued		
REAGENT or RESOURCE	SOURCE	IDENTIFIER
vclb – Reverse wt: GCATGATCACCAGATGGG	This paper	N/A
vclb – Forward mutant: CCCAGCAGATCTGGTGAT	This paper	N/A
Recombinant DNA		
kdrl:mCherry-vinculin plasmid	This paper	N/A
Software and algorithms		
JACoP plugin	Bolte and Cordelières, 2006	JACoP (Just Another Colocalization Plugin) (nih.gov)
ImageJ	N/A	https://imagej.nih.gov/ij/
MATLAB code for blood flow measurements		https://github.com/Jianmin-YIN/Blood-flow-measurement
Adobe Illustrator V 26.0.3	N/A	N/A
GraphPad Prism V 9.3.1	N/A	N/A

RESOURCE AVAILABILITY

Lead contact
Further information and request for resources and reagents should be directed and will be fulfilled by the Lead Contact; Heinz-Georg Belting (heinz-georg.belting@unibas.ch).

Materials availability
Materials and zebrafish lines generated and used in this study are available upon request to the lead contact.

Data and code availability
- Microscopy data reported in this paper will be shared by the lead contact upon request.
- All original code for blood flow measurements has been deposited at github (https://github.com/Jianmin-YIN/Blood-flow-measurement) and is publicly available. DOIs are listed in the key resources table.
- Any additional information required to reanalyze the data reported in this paper is available from the lead contact upon request.

EXPERIMENTAL MODEL AND SUBJECT DETAILS

Zebrafish lines and maintenance
Zebrafish were maintained in standard conditions (Aleström et al., 2019). All experiments were performed in accordance with federal guidance and approved by the Kantonales Veterinäramt of Kanton Basel-Stadt. The vcla[hu10818];vclb[hu11202] (Han et al., 2017) zebrafish lines were crossed into the following transgenic lines: *Tg(fli1a:EGFP)[y1]* (Lawson and Weinstein, 2002); *Tg(gata1a:dsRed)[sd2]* (Traver et al., 2003); *Tg(fli1a:pecam1a-EGFP)[ncv27]* (Ando et al., 2016); *Tg(fli1a:GFF)[ubs3]* and *Tg(UAS:EGFP-hZO1)[ubs5]* (Herwig et al., 2011); *(Tg(UAS:mRuby2-UCHD)[ubs20]* (Paatero et al., 2018); *Tg(kdrl:EGFP-nls)[ubs1]* (Blum et al., 2008); *Tg(kdrl:mCherry-CAAX)[s916]* (Hogan et al., 2009); *Tg(fli1a:Lifeact-EGFP)* (Phng et al., 2013), *TgBAC(ve-cad:ve-cadTS)[uq11bh]* (Lagendijk et al., 2017). Experiments were performed between 24 h postfertilization (hpf) and 48 hpf. Before imaging, embryos were selected for fluorescent signal. After imaging of the vinculin mutants, genotype was assessed by DNA extraction and PCR.

METHOD DETAILS

Genotyping of the vcl mutant lines
Genomic DNA from fin biopsies from adult fish or whole embryos was extracted by incubating the biopsies with NaOH at a final concentration of 50 mM and incubated for 10 min at 95°C. Subsequently, 1/10th of 1M Tris HCl pH 8 was added (Meeker et al., 2007). Finally, samples were treated with proteinase K for 1 h at 37°C and then for 5 min at 95°C to stop the proteinase K activity. Genomic DNA was then used to genotype the *vcla* and *vclb* loci. For genotyping analysis, four different primers were used to distinguish between wild-type, heterozygous or homozygous *vcla* or *vclb* alleles. For *vcla*, a combination of four primers (FP 5′-AGCTGATGATCT GAATCAGGTGTG-3′, RP 5′-TCGTTCAATCACTCGTGCAAACAG-3′, Fwd-wt 5′-ACCATGGAGGACTTGATCACT-3′, Rev-mut 5′-GGTCCCAGGTTTTTAGTGTAAGT-3′) and a PCR protocol including denaturation at 95°C for 30s, annealing at 52°C for 15s, extension at 68°C for 50s, 35 cycles and OneTaq DNA polymerase (NEB), generated PCR products of 497 bp and 203 bp for the wild-type allele, three PCR products of 497 bp, 282 bp and 203 bp for the heterozygous *vcla* mutants and for two PCR products of 497 bp and

282 bp for *vcla* homozygous mutants. For *vclb*, a combination of four primers (FP 5′-CGGTAGTTAGTTAGTTGTAGAGGGA GTC-3′, RP 5′-AATGAGAAAGCCTGAATGTGCG-3′, Rev-wt 5′-GCATGATCACCAGATGGG-3′, Fwd-mut 5′-CCCAGCAGATCTGG TGAT-3′) and a PCR protocol, including denaturation at 95°C for 30s, annealing at 49°C for 15s, extension at 68°C for 50s, 35 cycles and OneTaq DNA polymerase (NEB), generated two PCR products of 490 bp and 201 bp for the wild-type allele, PCR products of 490 bp, 319 bp and 201 for the heterozygous *vclb* mutant allele and PCR products of 490 bp and 319 bp for homozygous *vclb* mutant allele. PCR products were then loaded on a 1% agarose gel to assess the genotype (see Figures S4D and S4E).

Generation of kdrl:mCherry-vinculin expression plasmid

The *kdrl* promoter (Genbank accession number: AY045466) was subcloned in the tol2 transposon plasmid pDB739 (Balciunas et al., 2006) using the restriction sites BamHI and EcoRV. The N-terminal tagged mCherry-vinculin open reading frame (Twiss et al., 2012) was then inserted into the EcoRV restriction site adjacent to the kdrl promoter.

Embryo microinjections

For transient expression of the *kdrl:mCherry-vinculin*, plasmid DNA was injected into *Tg(fli1a:pecam1a-EGFP)^{ncv27}* or vcla^{hu10818};vclb^{hu11202}Tg(fli1a:pecam1a-EGFP)^{ncv27} embryos using a standard microinjection protocol (Lenard et al., 2013). Briefly, 1- to 2-cell stage embryos were placed on agarose matrices in E3 medium (5 mM NaCl, 0.17 mM KCl, 0.33 mM CaCl2, 0.33 mM MgSO4, pH 7.4) containing 5ppm methylene blue (Sigma) and were injected using glass microcapillaries (Biomedical instruments) and a WPI PV820 microinjector under a standard stereo microscope (Leica M80). 28 h after injection, embryos expressing EGFP and mCherry were selected using a Leica MI65FC fluorescent stereomicroscope, mounted in 0.7% low-melting point agarose and imaged using a Zeiss LSM880 confocal microscope as described below.

Immunofluorescence

Immunofluorescence staining of embryos was performed as previously described (Herwig et al., 2011) with few modifications. Briefly, embryos were fixed in 2% PFA in PBST (0.2% tween in PBS) and incubated overnight at 4°C. Embryos were washed in PBST and consecutively permeabilized in 0.5% Triton/PBST for 30-45 min at room temperature, and subsequently incubated in blocking solution (1% BSA, 0.2% Triton, 5% Goat Serum, 0.01% sodium azide in PBST) overnight at 4°C. Embryos were stained with mouse-anti-human-ZO-1 1:500 (Thermo Fisher Scientific, 33-9100), guinea pig-anti-zebrafish-VE-cadherin 1:500 (Paatero et al., 2018) or mouse anti-vinculin 1:500 antibodies (Sigma, V9131, Huveneers et al., 2012) diluted in Pierce Immunostain Enhancer medium (Thermo Fisher Scientific). Upon PBST washes, embryos were incubated with secondary antibodies, Alexa Fluor 405 goat anti-mouse immunoglobulin (IgG) 1:500 (Thermo Fisher Scientific), Alexa Fluor 568 goat anti-guinea pig IgG 1:500 (Thermo Fisher Scientific) or Alexa Fluor 405 goat anti-rabbit pig IgG 1:500 (Thermo Fisher Scientific).

Pharmacological treatments

To reduce heartbeat and inhibit blood circulation, we treated zebrafish embryos with 4x tricaine (0.32%, Sigma) in E3 embryo medium with 0.003% PTU (Sigma), as previously described (Lenard et al., 2013). To increase heartbeat and blood flow, we treated zebrafish embryos with 60 μM norepinephrine (Sigma) in E3 containing 0.003% PTU, as previously described (Chen et al., 2012; De Luca et al., 2014). Treatment of tricaine or norepinephrine started directly during imaging as indicated in the corresponding figures at 30-32 hpf. To perturb the actin cytoskeleton, embryos were treated with Latrunculin B (Sigma) using concentrations between 0.15 μg/mL to 0.6 μg/ml. A concentration of 0.15 μg/mL is sufficient to disrupt filopodia formation as previously described (Phng et al., 2013).

Imaging and image analysis

Fixed or live embryos were selected for fluorescence signal, anesthetized in E3 with 1x tricaine (0.08%, pH 7, Sigma) and mounted in glass bottom Petri dishes (MatTek) using 0.7% low-melting-point agarose (Sigma) containing 1x tricaine. For live-imaging, E3 with 1x tricaine and 0.003% 1-phenyl-2-thiourea (PTU, Sigma) to avoid pigmentation, was added to the dish. A Zeiss LSM880 Airy scan inverted confocal microscope was used for live-imaging and imaging of fixed samples. For fixed samples, the 40x (NA = 1.2) silicon oil immersion objective was used. Z-stacks were made with a step size of 0.5 μm. For live imaging, the 25x oil (NA = 0.8) or 40x silicon oil (NA = 1.2) immersion objectives were used. Images were acquired with a zoom of 1-1.6 and z-stacks were made with a step size of 0.5–1.0 μm. Frames were acquired every 5-30 min. High-resolution time-lapse images were acquired with an Olympus SpinSR spinning disc microscope using a 30x (NA = 1.05) oil objective (Photometrics). Frames were acquired every 1-2 min with a z stack step size of 0.7 μm. Confocal and Spinning disc images were analyzed using the Fiji/ImageJ software. For heartbeat and blood flow velocity, high-speed image acquisition was achieved using an iPhone 7 Camera at 120fps in conjunction with a Labcam adaptor connected to a Zeiss stereomicroscope (Stemi SV 11). Then velocity of blood flow was measured by tracing the movement of blood cells at the dorsal aorta using Particle Image Velocimetry (PIV) in combination with a homemade MATLAB code. The heart beat cycle was determined by the periodic oscillation of blood flow velocity at the dorsal aorta.

QUANTIFICATION AND STATISTICAL ANALYSIS

For analysis of blood vessel length, an average of three measurements was taken for each ISV and for analysis of blood vessel diameter, an average of three measurements was taken at different levels of each ISV. For analysis of the finger number, averages were taken for each ISV and junctional finger size was traced in three measurements per finger and averaged per ISV. For co-localization analysis, we subtracted the background (rolling ball radius 25) and selected regions of interests at junctional fingers. Co-localization analysis was performed using the Fiji software with the JACoP plugin. For gene expression levels of *vcla*, *vclb* and *ve-cadherin* in ECs versus non-ECs, analysis was performed using the transcriptome dataset from Lawson et al. (Lawson et al., 2020). Microsoft Excel was used for data analysis and Prism Graphpad V6 was used for statistical analysis and data visualization. Statistical parameters are reported in the figure legends. Violin plots represent median ± quartiles. When two groups were compared, a Student's T and one-way ANOVA (Kruskal-Wallis) tests were used. An analysis of variance (ANOVA) was used when more than two groups were compared to the control, in combination with a Dunnett's test for multiple comparisons and a D'Agostino-Pearson test for normality. Asterisks indicate p values, and are defined as ns = non-significant, $*p < 0.05$, $**p < 0.01$, $***p < 0.001$.